

# Virtual Compton Scattering and Neutral Pion Electroproduction in the Resonance Region up to the Deep Inelastic Region at Backward Angles

G. Laveissière,<sup>1</sup> N. Degrande,<sup>2</sup> S. Jaminion,<sup>1</sup> C. Jutier,<sup>1,3</sup> L. Todor,<sup>3</sup> R. Di Salvo,<sup>1</sup> L. Van Hoorebeke,<sup>2</sup> L.C. Alexa,<sup>4</sup> B.D. Anderson,<sup>5</sup> K.A. Aniol,<sup>6</sup> K. Arundell,<sup>7</sup> G. Audit,<sup>8</sup> L. Auerbach,<sup>9</sup> F.T. Baker,<sup>10</sup> M. Baylac,<sup>8</sup> J. Berthot,<sup>1</sup> P.Y. Bertin,<sup>1</sup> W. Bertozzi,<sup>11</sup> L. Bimbot,<sup>12</sup> W.U. Boeglin,<sup>13</sup> E.J. Brash,<sup>4</sup> V. Breton,<sup>1</sup> H. Breuer,<sup>14</sup> E. Burtin,<sup>8</sup> J.R. Calarco,<sup>15</sup> L.S. Cardman,<sup>16</sup> C. Cavata,<sup>8</sup> C.-C. Chang,<sup>14</sup> J.-P. Chen,<sup>16</sup> E. Chudakov,<sup>16</sup> E. Cisbani,<sup>17</sup> D.S. Dale,<sup>18</sup> C.W. de Jager,<sup>16</sup> R. De Leo,<sup>19</sup> A. Deur,<sup>1,16</sup> N. d'Hose,<sup>8</sup> G.E. Dodge,<sup>3</sup> J.J. Domingo,<sup>16</sup> L. Elouadrhiri,<sup>16</sup> M.B. Epstein,<sup>6</sup> L.A. Ewell,<sup>14</sup> J.M. Finn,<sup>7</sup> K.G. Fissum,<sup>11</sup> H. Fonvieille,<sup>1,\*</sup> G. Fournier,<sup>8</sup> B. Frois,<sup>8</sup> S. Frullani,<sup>17</sup> C. Furget,<sup>20</sup> H. Gao,<sup>11</sup> J. Gao,<sup>11</sup> F. Garibaldi,<sup>17</sup> A. Gasparian,<sup>21,18</sup> S. Gilad,<sup>11</sup> R. Gilman,<sup>22,16</sup> A. Glamazdin,<sup>23</sup> C. Glashauser,<sup>22</sup> J. Gomez,<sup>16</sup> V. Gorbenko,<sup>23</sup> P. Grenier,<sup>1</sup> P.A.M. Guichon,<sup>8</sup> J.O. Hansen,<sup>16</sup> R. Holmes,<sup>24</sup> M. Holtrop,<sup>15</sup> C. Howell,<sup>25</sup> G.M. Huber,<sup>4</sup> C.E. Hyde,<sup>3,1</sup> S. Incerti,<sup>9</sup> M. Iodice,<sup>17</sup> J. Jardillier,<sup>8</sup> M.K. Jones,<sup>7</sup> W. Kahl,<sup>24</sup> S. Kamalov,<sup>26</sup> S. Kato,<sup>27</sup> A.T. Katramatou,<sup>5</sup> J.J. Kelly,<sup>14</sup> S. Kerhoas,<sup>8</sup> A. Ketikyan,<sup>28</sup> M. Khayat,<sup>5</sup> K. Kino,<sup>29</sup> S. Kox,<sup>30</sup> L.H. Kramer,<sup>13</sup> K.S. Kumar,<sup>31</sup> G. Kumbartzki,<sup>22</sup> M. Kuss,<sup>16</sup> A. Leone,<sup>32</sup> J.J. LeRose,<sup>16</sup> M. Liang,<sup>16</sup> R.A. Lindgren,<sup>33</sup> N. Liyanage,<sup>11</sup> G.J. Lolos,<sup>4</sup> R.W. Lourie,<sup>34</sup> R. Madey,<sup>5</sup> K. Maeda,<sup>29</sup> S. Malov,<sup>22</sup> D.M. Manley,<sup>5</sup> C. Marchand,<sup>8</sup> D. Marchand,<sup>8</sup> D.J. Margaziotis,<sup>6</sup> P. Markowitz,<sup>13</sup> J. Marroncle,<sup>8</sup> J. Martino,<sup>8</sup> K. McCormick,<sup>3</sup> J. McIntyre,<sup>22</sup> S. Mehrabyan,<sup>28</sup> F. Merchez,<sup>30</sup> Z.E. Meziani,<sup>9</sup> R. Michaels,<sup>16</sup> G.W. Miller,<sup>31</sup> J.Y. Mougey,<sup>30</sup> S.K. Nanda,<sup>16</sup> D. Neyret,<sup>8</sup> E.A.J.M. Offermann,<sup>16</sup> Z. Papandreou,<sup>4</sup> C.F. Perdrisat,<sup>7</sup> R. Perrino,<sup>32</sup> G.G. Petratos,<sup>5</sup> S. Platchkov,<sup>8</sup> R. Pomatsalyuk,<sup>23</sup> D.L. Prout,<sup>5</sup> V.A. Punjabi,<sup>35</sup> T. Pussieux,<sup>8</sup> G. Quémenér,<sup>1,7</sup> R.D. Ransome,<sup>22</sup> O. Ravel,<sup>1</sup> J.S. Real,<sup>30</sup> F. Renard,<sup>8</sup> Y. Roblin,<sup>1</sup> D. Rowntree,<sup>11</sup> G. Rutledge,<sup>7</sup> P.M. Rutt,<sup>22</sup> A. Saha,<sup>16</sup> T. Saito,<sup>29</sup> A.J. Sarty,<sup>36</sup> A. Serdarevic,<sup>4,16</sup> T. Smith,<sup>15</sup> G. Smirnov,<sup>1</sup> K. Soldi,<sup>37</sup> P. Sorokin,<sup>23</sup> P.A. Souder,<sup>24</sup> R. Suleiman,<sup>11</sup> J.A. Templon,<sup>10</sup> T. Terasawa,<sup>29</sup> L. Tiator,<sup>26</sup> R. Tieulent,<sup>30</sup> E. Tomasi-Gustafsson,<sup>8</sup> H. Tsubota,<sup>29</sup> H. Ueno,<sup>27</sup> P.E. Ulmer,<sup>3</sup> G.M. Urciuoli,<sup>17</sup> R. Van De Vyver,<sup>2</sup> R.L.J. Van der Meer,<sup>16,4</sup> P. Vernin,<sup>8</sup> B. Vlahovic,<sup>16,37</sup> H. Voskanyan,<sup>28</sup> E. Voutier,<sup>30</sup> J.W. Watson,<sup>5</sup> L.B. Weinstein,<sup>3</sup> K. Wijesooriya,<sup>7</sup> R. Wilson,<sup>38</sup> B.B. Wojtsekhowski,<sup>16</sup> D.G. Zainea,<sup>4</sup> W-M. Zhang,<sup>5</sup> J. Zhao,<sup>11</sup> and Z.-L. Zhou<sup>11</sup>

(The Jefferson Lab Hall A Collaboration)

<sup>1</sup>LPC-Clermont, Université Blaise Pascal, CNRS/IN2P3, F-63177 Aubière Cedex, France

<sup>2</sup>University of Gent, B-9000 Gent, Belgium

<sup>3</sup>Old Dominion University, Norfolk, VA 23529

<sup>4</sup>University of Regina, Regina, SK S4S 0A2, Canada

<sup>5</sup>Kent State University, Kent OH 44242

<sup>6</sup>California State University, Los Angeles, Los Angeles, CA 90032

<sup>7</sup>College of William and Mary, Williamsburg, VA 23187

<sup>8</sup>CEA Saclay, F-91191 Gif-sur-Yvette, France

<sup>9</sup>Temple University, Philadelphia, PA 19122

<sup>10</sup>University of Georgia, Athens, GA 30602

<sup>11</sup>Massachusetts Institute of Technology, Cambridge, MA 02139

<sup>12</sup>IPNO, Université Paris XI, CNRS/IN2P3, F-91406 Orsay, France

<sup>13</sup>Florida International University, Miami, FL 33199

<sup>14</sup>University of Maryland, College Park, MD 20742

<sup>15</sup>University of New Hampshire, Durham, NH 03824

<sup>16</sup>Thomas Jefferson National Accelerator Facility, Newport News, VA 23606

<sup>17</sup>INFN, Sezione Sanità and Istituto Superiore di Sanità, 00161 Rome, Italy

<sup>18</sup>University of Kentucky, Lexington, KY 40506

<sup>19</sup>INFN, Sezione di Bari and University of Bari, 70126 Bari, Italy

<sup>20</sup>LPSC Grenoble, Université Joseph Fourier, CNRS/IN2P3, INP, F-38026 Grenoble, France

<sup>21</sup>Hampton University, Hampton, VA 23668

<sup>22</sup>Rutgers, The State University of New Jersey, Piscataway, NJ 08855

<sup>23</sup>Kharkov Institute of Physics and Technology, Kharkov 61108, Ukraine

<sup>24</sup>Syracuse University, Syracuse, NY 13244

<sup>25</sup>Duke University, Durham, NC 27706

<sup>26</sup>Institut fuer Kernphysik, University of Mainz, D-55099 Mainz, Germany

<sup>27</sup>Yamagata University, Yamagata 990, Japan

<sup>28</sup>Yerevan Physics Institute, Yerevan 375036, Armenia

<sup>29</sup>Tohoku University, Sendai 980, Japan

<sup>30</sup>LPSC, Université Joseph Fourier, CNRS/IN2P3, F-38026 Grenoble, France

<sup>31</sup>Princeton University, Princeton, NJ 08544

<sup>32</sup>INFN, Sezione di Lecce, 73100 Lecce, Italy

<sup>33</sup>University of Virginia, Charlottesville, VA 22901

<sup>34</sup>State University of New York at Stony Brook, Stony Brook, NY 11794

<sup>35</sup>Norfolk State University, Norfolk, VA 23504

<sup>36</sup>Florida State University, Tallahassee, FL 32306

<sup>37</sup>North Carolina Central University, Durham, NC 27707

<sup>38</sup>Harvard University, Cambridge, MA 02138

We have made the first measurements of the virtual Compton scattering (VCS) process via the  $H(e, e'p)\gamma$  exclusive reaction in the nucleon resonance region, at backward angles. Results are presented for the  $W$ -dependence at fixed  $Q^2 = 1 \text{ GeV}^2$ , and for the  $Q^2$ -dependence at fixed  $W$  near 1.5 GeV. The VCS data show resonant structures in the first and second resonance regions. The observed  $Q^2$ -dependence is smooth. The measured ratio of  $H(e, e'p)\gamma$  to  $H(e, e'p)\pi^0$  cross sections emphasizes the different sensitivity of these two reactions to the various nucleon resonances. Finally, when compared to Real Compton Scattering (RCS) at high energy and large angles, our VCS data at the highest  $W$  (1.8-1.9 GeV) show a striking  $Q^2$ -independence, which may suggest a transition to a perturbative scattering mechanism at the quark level.

PACS numbers: 13.60.Fz, 25.30.Rw

## I. INTRODUCTION

Understanding nucleon structure in terms of the non-perturbative dynamics of quarks and gluons requires new and diverse experimental data to guide theoretical approaches and to constrain models. Purely electro-weak processes are privileged tools since they can be interpreted directly in terms of the current carried by the quarks. This paper presents a study of the virtual Compton scattering (VCS) process :  $\gamma^*p \rightarrow \gamma p$ , in the nucleon resonance region via the photon electroproduction reaction :  $H(e, e'p)\gamma$ , together with results in the neutral pion electroproduction channel  $H(e, e'p)\pi^0$ . This study is based on part of the data of the E93-050 experiment [1, 2] performed at the Thomas Jefferson National Accelerator Facility (JLab). Its motivations were twofold: 1) investigate the very low-energy region, below the pion production threshold, to determine the Generalized Polarizabilities of the proton [1]; 2) make an exploratory study of the VCS process in the region of the nucleon resonances, which is the subject of the present paper. A first set of E93-050 results in the  $H(e, e'p)\pi^0$  channel were published in [2]. This experiment was part of the Hall A commissioning phase, and was therefore conducted prior to the Real Compton Scattering (RCS) and Deep VCS (DVCS) program at JLab. Lastly, in this experiment the photon electroproduction process was for the first time cleanly separated from the dominant  $H(e, e'p)\pi^0$  reaction above pion threshold.

The Constituent Quark Model of Isgur and Karl [3, 4] reproduces many features of the nucleon spectrum. However, the structure of the nucleon resonances, particularly the electro-weak transition form factors, remain incompletely understood. The simultaneous study of both  $(N\pi)$  and  $(N\gamma)$  final states of the electroproduction process on the nucleon offers probes with very different sen-

sitivities to the resonance structures. Another motivation for the present study is to explore the exclusive  $H(e, e'p)\gamma$  reaction at high  $W$ , where perturbative current quark degrees of freedom may become as important as those of constituent quarks and resonances. Quark-hadron duality implies that even at modest  $Q^2$ , inelastic electron scattering in the resonance region can be analyzed in terms of quark rather than nucleon resonance degrees of freedom [5].

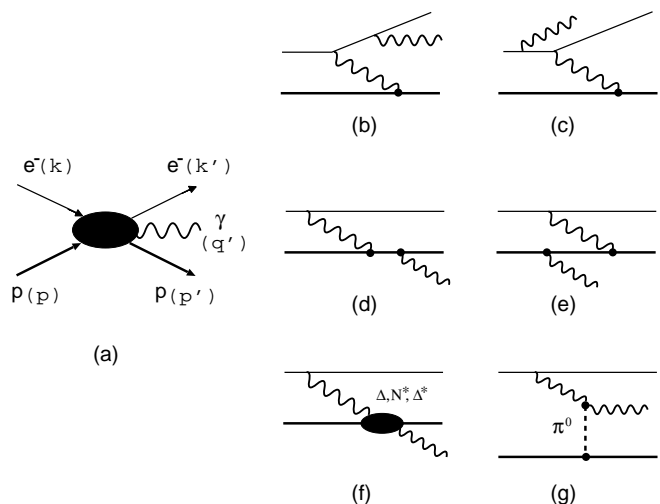


FIG. 1: Kinematics for photon electroproduction on the proton (a) and lowest order amplitudes for Bethe-Heitler (b, c), VCS Born (d, e), VCS Non-Born (f), and  $t$ -channel  $\pi^0$ -exchange (g) processes. The particle four-momenta are indicated in parenthesis in a).

### A. Kinematics

The kinematics of the  $H(e, e'p)\gamma$  reaction are represented in Fig. 1a. A common set of invariant kinematic variables is defined as  $-Q^2 = (k - k')^2 = q^2$ ,

\*e-mail: helene@clermont.in2p3.fr

$s = W^2 = (q + p)^2$ ,  $t = (p - p')^2$ , and  $u = (p - q')^2$ . The  $\vec{q}$ -direction defines the polar axis of the coordinate system:  $\theta_{\gamma\gamma}^*$  and  $\phi$  are the polar and azimuthal angles in the  $\gamma^*p \rightarrow \gamma p$  subprocess c.m. frame. The scattered electron direction defines  $\phi = 0$ . The  $H(e, e'p)\gamma$  reaction was measured below the pion threshold in several experiments [1, 6, 7, 8] and in the region of the  $\Delta(1232)$  resonance [9, 10].

We present in this paper the first measurements of the  $H(e, e'p)\gamma$  cross section that were made through the entire nucleon resonance region. We measured the photon electroproduction cross section in two scans:

- The nucleon excitation function from threshold to  $W = 1.9$  GeV at  $Q^2 = 1$  GeV<sup>2</sup>;
- The  $Q^2$ -dependence near  $W = 1.5$  GeV.

The cross section for the  $H(e, e'p)\pi^0$  process was determined simultaneously in the experiment, at the same kinematics. All these measurements were performed in backward kinematics, i.e. within a cone ( $\cos\theta_{\gamma\gamma}^* < -0.5$ ) centered on the backward axis ( $\vec{q}'$  opposite to  $\vec{q}$ ). This angular domain, traditionally dominated by  $u$ -channel exchanges, is opposite to the DVCS kinematics which are at forward  $\theta_{\gamma\gamma}^*$ .

### B. Interference of Bethe-Heitler and VCS Amplitudes

In the one-photon exchange approximation, the photon electroproduction amplitude (Fig. 1a) includes the coherent superposition of the VCS Born (Fig. 1d and 1e) and Non-Born (Fig. 1f) amplitudes, and the Bethe-Heitler (BH) one (Fig. 1b and 1c) [11]. Note that in the BH amplitude, the mass-squared of the virtual photon (elastically absorbed by the proton) is  $t$ . In the VCS amplitude, the mass-squared of the virtual photon (inelastically absorbed) is  $-Q^2$ . The BH amplitude dominates over VCS when the photon is emitted in either the direction of the incident or scattered electron. It also breaks the symmetry of the electroproduction amplitude around the virtual photon direction. Thus, in the data analysis we have not expanded the  $\phi$ -dependence of the  $H(e, e'p)\gamma$  cross section in terms of the usual electroproduction  $LT$  and  $TT$  interference terms. This would be possible for  $W$  well above the  $\Delta(1232)$ -resonance, where the BH amplitude becomes negligible. However, in this region ( $W \geq 1.4$  GeV) our data are mostly  $\phi$ -independent within statistics.

## II. EXPERIMENT AND ANALYSIS

We performed the experiment at JLab in Hall A. The continuous electron beam of energy 4.032 GeV with an intensity of 60-120  $\mu$ A bombarded a 15 cm liquid hydrogen target. The scattered electron and recoil proton were

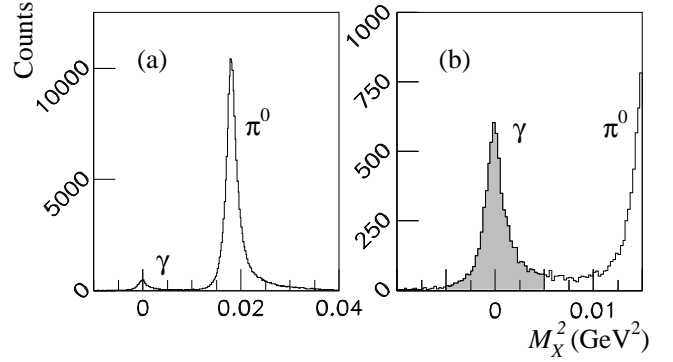


FIG. 2: Squared missing mass  $M_X^2$  for an experimental setting at  $W = 1.2$  GeV (a) and zoom around the  $\gamma$  peak (b). The shaded window  $[-0.005, 0.005]$  GeV<sup>2</sup> is used to select the  $\gamma$  events. The FWHM of the peak increases from 0.0022 to 0.0050 GeV<sup>2</sup> when  $W$  goes from 1.1 to 1.9 GeV.

detected in coincidence in two high-resolution spectrometers. The emitted photon or  $\pi^0$  was identified by reconstruction of the mass of the missing particle. A spectrum of the squared missing mass  $M_X^2 = (k + p - k' - p')^2$  is displayed in Fig. 2 and shows the good resolution achieved in the separation of the two electroproduction channels. The apparatus is described in detail in [12], and the detector acceptance and spectrometer settings in [2].

We extract the five-fold differential cross section  $d^5\sigma(ep \rightarrow ep\gamma) = d^5\sigma/(dk'_{lab} d[\Omega_e]_{lab} d[\Omega_p]_{c.m.})$  using the method described in [2];  $dk'_{lab}$  and  $d[\Omega_e]_{lab}$  are the scattered electron differential momentum and solid angle in the lab frame, and  $d[\Omega_p]_{c.m.}$  is the proton c.m. differential solid angle. The calculations of the solid angle and radiative corrections are based on a simulation [13] including the coherent sum of the BH and VCS-Born amplitudes (Fig. 1b,c,d and e) only. The inclusion of the BH-amplitude ensures that our simulation reproduces the strong  $\phi$ -dependence near pion threshold. Corrections were applied for acceptance, trigger efficiency, acquisition and electronic dead times, tracking efficiency, target boiling, target impurity and proton absorption [2]. In addition, a correction ( $-0.1$  to  $-1.7\%$ ) for the exclusive  $\pi^0$  background in the  $M_X^2$  window  $[-0.005, 0.005]$  GeV<sup>2</sup> was made using our simulation, based on the results of [2].

The data are binned in the variables  $\cos\theta_{\gamma\gamma}^*$ ,  $\phi$  and  $W$ . In each bin the cross section is determined at a fixed point, using the model dependence of the BH+Born calculation. This fixed point is at the center of the bins in  $\cos\theta_{\gamma\gamma}^*$ ,  $\phi$  and  $W$ . We define three bins in  $\cos\theta_{\gamma\gamma}^*$ :  $[-1.0, -0.95]$ ,  $[-0.95, -0.80]$ , and  $[-0.80, -0.50]$ , therefore the cross section is determined at  $\cos\theta_{\gamma\gamma}^* = -0.975, -0.875$  and  $-0.650$ . The phase space in  $\phi$  is divided in six bins from  $0^\circ$  to  $180^\circ$ , of  $30^\circ$  width. The statistics from  $\phi = -180^\circ$  to  $\phi = 0^\circ$  are added using the symmetry property of the unpolarized cross section w.r.t. to the lepton plane,  $d\sigma(\phi) = d\sigma(2\pi - \phi)$ . The elementary bin size in  $W$  is 20 MeV.

The two other variables needed to complete the kinematics are the photon virtuality  $Q^2$  (constant in the first scan and variable in the second scan) and the beam energy in the lab, which is always kept fixed:  $k_{lab} = 4.032$  GeV. As a consequence, the virtual photon polarization  $\epsilon = [1 + 2(\vec{q}^2/Q^2) \tan^2(\theta_e/2)]^{-1}$  is not constant but decreases monotonically from 0.95 at  $W=1$  GeV to 0.75 at  $W=1.9$  GeV.

Full results, including statistical and instrumental uncertainties are presented in the Tables of the Appendix. The cross-section values are statistically independent, bin-to-bin. Systematic errors on the cross section are studied in [14]. They mainly originate from uncertainties in the absolute normalization (integrated beam charge), the radiative corrections, and the knowledge of the experimental acceptance. They are mostly correlated bin-to-bin. Another source of systematic error is due to the physical background subtraction. It is mostly independent bin-to-bin in  $W$ , and it affects the  $\gamma$  channel more than the  $\pi^0$  channel (due to lower VCS statistics). As a result the total systematic error is larger in the  $\gamma$  channel than in the  $\pi^0$  channel (cf. the Tables of the Appendix).

The most detailed cross section is five-fold differential. However, for relevant studies we will use a two-fold cross section. Throughout this analysis the parametrization of ref. [15] is used for the proton electromagnetic form factors, namely to compute the BH+Born cross section. The next sections present our results.

### III. RESULTS

#### A. VCS Resonance Data, Scan in $W$ at $Q^2 = 1$ GeV<sup>2</sup>

This first scan provides an overall picture of the nucleon excitation spectrum induced by the electromagnetic probe, conditioned by the  $(\gamma p)$  specific de-excitation channel. Tables I to III contain the numerical values of the five-fold differential cross section  $d^5\sigma(ep \rightarrow ep\gamma)$  at  $Q^2 = 1$  GeV<sup>2</sup>, for the six bins in  $\phi$  as a function of  $W$ , and  $\cos\theta_{\gamma\gamma}^* = -0.975, -0.875, \text{ and } -0.650$ . In Fig. 3 we present this cross section in the most backward bin, at  $\cos\theta_{\gamma\gamma}^* = -0.975$ .

The strong rise that the data show towards very low  $W$  and  $\phi \sim 180^\circ$ , is due to the BH tail of elastic electron scattering. In this region there is obviously a strong interference between the BH and the VCS amplitudes, evolving from destructive at  $\phi = 15^\circ$  to constructive at larger  $\phi$ . The cross section calculated from the coherent sum of the BH and Nucleon-Born amplitudes (thin solid curve) is in excellent agreement with the data.

In the first resonance region, the thick solid curve shows the calculation based on Dispersion Relations (DR) by B.Pasquini *et al.* [17]. In this theoretical framework, our data were previously analyzed in terms of Generalized Polarizabilities for  $W < 1.28$  GeV [1]. The DR

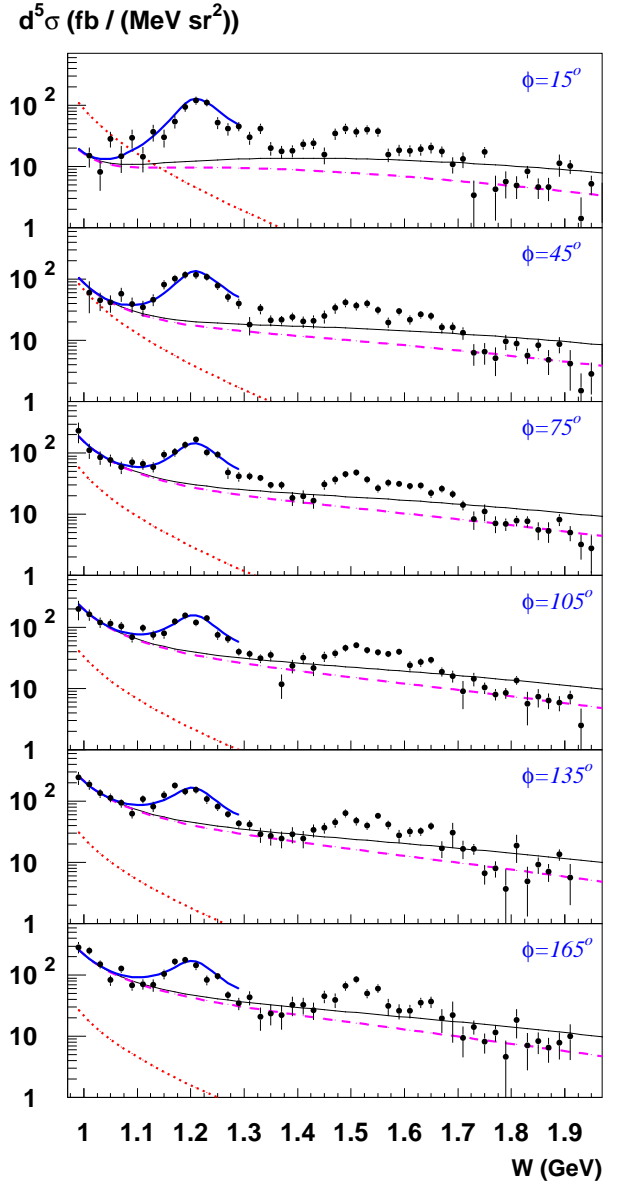


FIG. 3: (Color online) Excitation curves for the  $H(e, e'p)\gamma$  reaction at  $Q^2 = 1$  GeV<sup>2</sup>,  $\cos\theta_{\gamma\gamma}^* = -0.975$ ,  $k_{lab} = 4.032$  GeV and six values of  $\phi$ , as marked. The thick solid curve up through the  $\Delta$ -resonance is our DR fit of the Generalized Polarizabilities [1]. The thin solid curve is the BH+Born cross section, and the dashed curve is the BH+Born+ $\pi^0$ -exchange cross section [16]. The dotted curve is the pure Bethe-Heitler cross section.

model is able to predict the 12 independent VCS scattering amplitudes, in terms of the  $\gamma^*N \rightarrow N\pi$  multipoles,  $t$ -channel  $\pi^0$  exchange, and two phenomenological functions:  $\Delta\alpha(Q^2)$  and  $\Delta\beta(Q^2)$ . These two functions parameterize the contributions to the electric and magnetic polarizabilities from high-energy virtual channels. In particular, the term  $\Delta\beta(Q^2)$  is modeled by  $t$ -channel  $\sigma$ -meson exchange. In [18], it was suggested that

the combination  $[\Delta\alpha + \Delta\beta](Q^2)$  is likely dominated by the  $N\pi\pi$  and  $N\eta$  multipoles, which are not presently included in the DR formalism. When a comprehensive partial wave analysis of the  $\gamma^*N \rightarrow N\pi\pi$  multipoles becomes available, the DR formalism could be extended to the second resonance region ( $W \approx 1.5$  GeV). A comparison with the present data would improve our understanding of the spatial distribution of the polarization response of the proton, by identifying more explicitly which channels and excitations contribute to the Generalized Polarizabilities.

In Fig. 3 we also see strong resonance phenomena in the second resonance region. The higher resonances are not distinguishable, due to a combination of the limited statistical precision and the interference of many open channels in the intermediate state of the VCS amplitude. For  $W > 1.3$  GeV, there is no complete model calculation of VCS incorporating resonances. Nevertheless, the data follow the general trend of the BH+Born calculation at high  $W$ , when we include the destructive  $t$ -channel  $\pi^0$  exchange graph [16] of Fig. 1g. This is somewhat surprising, given the spectrum of baryon resonances. In the resonance model of Capstick and Keister [19] for RCS, the positive-parity intermediate states contribute constructively and the negative-parity states contribute destructively to the backward-angle cross section. Although diffractive minima can cause some amplitudes to change sign with  $Q^2$ , this basic effect will remain in VCS. Thus the high-level density of resonances at large  $W$  does not necessarily enhance the backward cross section, and leads to a smooth behavior. In section III D, we explore the question of which degrees of freedom are essential for the high-energy backward Compton amplitude.

### B. $Q^2$ -Dependence in the Region of $W = 1.5$ GeV

A second set of data was taken in order to study the  $Q^2$ -dependence of the cross section at a fixed c.m. energy. Ideally, such data provide information on the transition form factors of the nucleon resonances. Here we have performed an exploratory scan in the second resonance region, around  $W = 1.53$  GeV, where the strongest excitations are the  $D_{13}(1520)$  and  $S_{11}(1535)$  resonances.

This study was performed for both channels  $H(e, e'p)\gamma$  and  $H(e, e'p)\pi^0$ . Measuring the two processes at the same kinematics allows to compare the sensitivity to the various resonances in two different exit channels.

The detailed  $Q^2$ -dependence of our experimental data is obtained by subdividing the spectrometer acceptance of three separate kinematic settings centered at  $Q^2 = 0.6$ , 1.0, and 2.0 GeV<sup>2</sup>. Tables IV to VII contain the differential cross section in each elementary bin in  $(Q^2, W, \phi)$ . For the figures we define a two-fold cross section. To this aim we first divide  $d^5\sigma$  by the virtual photon flux factor:

$$\frac{d^2\sigma}{d[\Omega_p]_{\text{c.m.}}} = \frac{d^5\sigma}{dk'_{lab} d[\Omega_e]_{lab} d[\Omega_p]_{\text{c.m.}}} \times \frac{1}{\Gamma}. \quad (1)$$

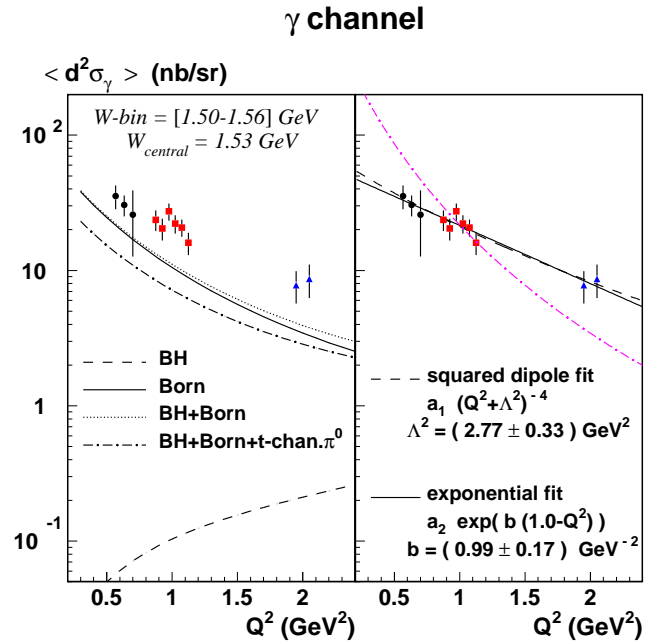


FIG. 4: (Color online) The  $Q^2$ -dependence of the reduced cross section  $\langle d^2\sigma_\gamma \rangle$  in photon electroproduction (see text), at fixed  $\cos\theta_{\gamma\gamma}^* = -0.975$ ,  $k_{lab} = 4.032$  GeV and  $W = 1.53$  GeV (statistical error only). The three different datasets are labelled by circles, squares and triangles. Left panel: comparison with theoretical calculations at  $W = 1.53$  GeV. Right panel: the same experimental points with two different types of fits, having  $(a_1, \Lambda^2)$  or  $(a_2, b)$  as free parameters. The dot-dashed curve is the standard nucleon dipole squared,  $G_D^2 = (1 + Q^2(\text{GeV}^2)/0.71)^{-4}$ , normalized arbitrarily to the data point at  $Q^2 = 1$  GeV<sup>2</sup>.

The flux factor (Hand convention [20]) is defined by:

$$\Gamma = \frac{\alpha}{2\pi^2} \cdot \frac{k'_{lab}}{k_{lab}} \cdot \frac{W^2 - M_p^2}{2M_p Q^2} \cdot \frac{1}{1 - \epsilon} \quad (2)$$

where  $\alpha$  is the fine structure constant and  $M_p$  the proton mass. We then extract the  $\phi$ -independent term of  $d^2\sigma/d[\Omega_p]_{\text{c.m.}}$ , which will be called reduced cross section and noted  $\langle d^2\sigma \rangle$ . Since in each small  $Q^2$ -bin the coverage in  $\phi$  is often not complete, this extraction is performed by fitting the experimental data to the  $\phi$ -dependence of a model. The chosen model is (BH+Born) for photon electroproduction and MAID2000 for pion electroproduction. We just fit a global scale parameter from model to experiment; then from this parameter and the model it is straightforward to determine  $\langle d^2\sigma \rangle$  in the bin. The data represented in Figs. 4 and 5 are given in Table VIII.

#### 1. The $H(e, e'p)\gamma$ Process

If the BH process was fully negligible, the obtained cross section  $\langle d^2\sigma_\gamma \rangle$  would represent the usual term

$d^2\sigma_T + \epsilon d^2\sigma_L$  of the VCS subprocess ( $\gamma^*p \rightarrow \gamma p$ ). However, this is only approximately true. In the kinematics considered here, the modulus of the BH amplitude still represents 6-15% of the modulus of the BH+Born amplitude.

In Fig. 4 we plot the  $Q^2$ -dependence of the reduced VCS cross section  $\langle d^2\sigma_\gamma \rangle$  at  $W = 1.53$  GeV and  $\cos\theta_{\gamma\gamma}^* = -0.975$ . A large bin width (60 MeV) is chosen in  $W$  in order to gain statistical accuracy. The measured values are a factor 2-3 above the BH+Born calculation, which may not be surprising since the model does not include any resonance structure. The  $Q^2$ -dependence of the data is rather smooth. It is well reproduced in relative by the (BH+Born) or the (BH+Born +  $t$ -channel  $\pi^0$ -exchange) calculation.

The data are well fitted by a dipole or an exponential behavior, as illustrated in the right panel of Fig. 4. We note that the dipole mass parameter  $\Lambda^2$  is much larger than for the standard nucleon dipole form factor  $G_D$ . Without doing a complete analysis in terms of helicity amplitudes of the resonances as in refs. [21] or [22], it is clear from our data that the involved transition form factors have a much slower decrease with  $Q^2$  than  $G_D$ , in the explored  $Q^2$ -range. Interpretation of these data will require a systematic treatment of both the on-shell and off-shell intermediate states, entering the imaginary and real parts of the VCS amplitude, respectively. Strong contributions to the real part of the VCS amplitude are expected from resonances distant in  $W$ .

## 2. The $H(e, e'p)\pi^0$ Process

In the  $\pi^0$  channel, the reduced cross section  $\langle d^2\sigma_{\pi^0} \rangle$  strictly corresponds to the  $\phi$ -independent term  $d^2\sigma_T + \epsilon d^2\sigma_L$  of pion electroproduction. The data at the  $Q^2 = 1$  GeV<sup>2</sup> setting were previously published in [2] (but without subdividing into small  $Q^2$ -bins).

Figure 5 shows the  $Q^2$ -dependence of the reduced cross section  $\langle d^2\sigma_{\pi^0} \rangle$  at the same kinematics as Fig. 4. The enhanced statistics in the  $\pi^0$  channel allow us to choose a smaller bin width in  $W$ , of 20 MeV. The observed  $Q^2$ -dependence is again rather smooth. Among the various versions of the MAID unitary isobar model [23], the most recent ones (2003 or 2007) better reproduce the  $Q^2$ -dependence of the data, however they still underestimate the cross section in absolute by  $\sim 20$ -30%. The SAID WI03K [24] curve is a global fit including our  $Q^2 = 1$  GeV<sup>2</sup> data [2], i.e. the points labelled by a square in Fig. 5. Therefore this model works well around  $Q^2 = 1$  GeV<sup>2</sup>, but gives poorer agreement with the data around  $Q^2 = 2$  GeV<sup>2</sup>. The most recent SAID calculation SM08 [25] is in good agreement with the data for  $Q^2 = 1$  and 2 GeV<sup>2</sup>.

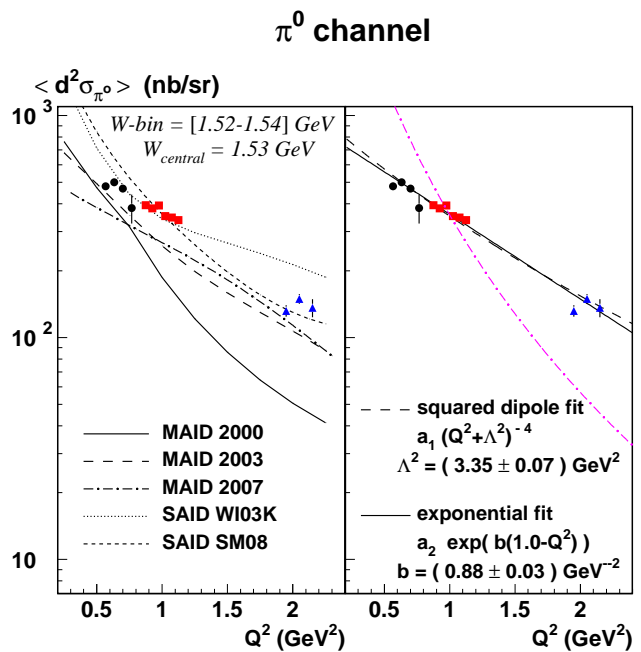


FIG. 5: (Color online) The  $Q^2$ -dependence of the reduced cross section  $\langle d^2\sigma_{\pi^0} \rangle$  in  $\pi^0$  electroproduction, at fixed  $\cos\theta_{\gamma\gamma}^* = -0.975$ ,  $k_{lab} = 4.032$  GeV and  $W = 1.53$  GeV (statistical error only). Left panel: comparison with theoretical calculations at  $W = 1.53$  GeV. Right panel: the same experimental points with two different types of fits. Same comments as in the previous figure.

## 3. $W$ -Dependence of the $Q^2$ -Dependence

From both inclusive and exclusive data, it is known [21] that in the second resonance region the virtual photo-absorption cross section is dominated by the  $D_{13}(1520)$  resonance at low  $Q^2$  ( $< 1$  GeV<sup>2</sup>), while for  $Q^2 > 2$  GeV<sup>2</sup> it is dominated by the  $S_{11}(1535)$  resonance. Furthermore, some of the transition multipoles of these two resonances do not have simple dipole shapes in  $Q^2$  [22]. This should result in a complicated  $Q^2$ -dependence of electroproduction cross sections. However, surprisingly, the behavior observed in Figs. 4 and 5 at  $W = 1.53$  GeV can be described by a single dipole fall-off.

To further explore the  $Q^2$ -behavior of our reduced cross sections, we have performed the same fits as in Figs. 4 and 5, i.e. dipolar or exponential, in each elementary  $W$ -bin of 20 MeV width, in the  $W$ -range [1.45, 1.59] GeV. The result is presented in Fig. 6. One first observes that the fitted parameters take globally the same value for the  $H(e, e'p)\gamma$  and  $H(e, e'p)\pi^0$  processes, i.e.  $\Lambda^2 \simeq 3$  GeV<sup>2</sup>, or  $b \simeq 0.9$  GeV<sup>-2</sup> everywhere. This slope value for  $b$  is intermediate between the values found for the  $S_{11}(1535)$  and the  $D_{13}(1520)$  resonances ( $b = 0.38$  and  $1.60$  GeV<sup>-2</sup>, respectively [26] (see also [27, 28])). Assuming that the  $Q^2$ -dependence of the virtual photo-production of a resonance is given only by the coupling ( $\gamma^*p \rightarrow$  resonance) and does not depend on the exit channel, then our  $\sim$  con-

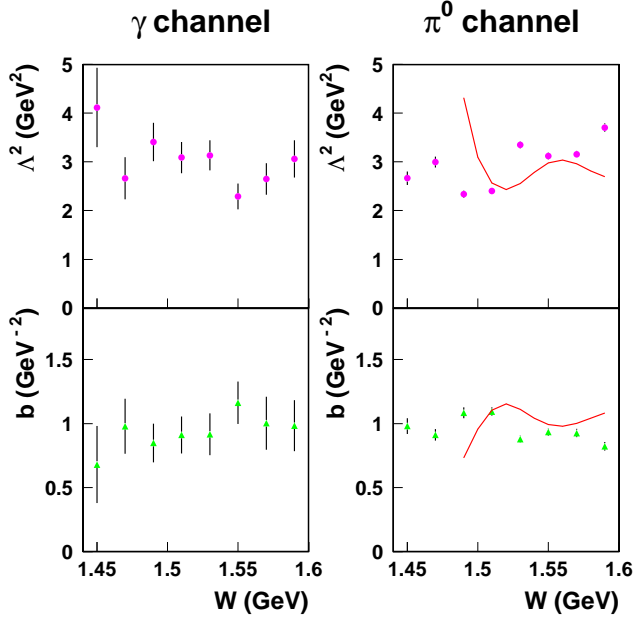


FIG. 6: (Color online) The slope parameters  $\Lambda^2$  and  $b$  introduced in the two previous figures, determined here in each elementary  $W$ -bin of width 20 MeV (statistical error only). Left and right panels are for photon and  $\pi^0$  electroproduction, respectively. The solid curve ( $\pi^0$  channel) gives the result of the MAID2003 calculation, limited to  $W \geq 1.49$  GeV. This is the only region in  $W$  for which the MAID calculation is well described by a simple dipole or exponential fit in the  $Q^2$ -range [0.5, 2.0] GeV<sup>2</sup>.

stant  $b$  suggests that approximately the “same mixing” of resonances is seen in the two exit channels ( $\gamma p$  or  $\pi^0 p$ ), in the explored  $W$ -range.

However, at a finer scale the data of Fig. 6 do show some variations with  $W$ , which appear to be non-trivial, and of opposite sign in the two exit channels  $\gamma p$  and  $\pi^0 p$ . Such variations are also present in model calculations, e.g. MAID2003 in the figure ( $\pi^0$  channel). One concludes that the competition from multiple resonance channels results in a complicated  $W$ -dependence of the  $Q^2$ -dependence of electroproduction cross sections.

Note that the  $b$  parameter of the exponential fit was determined previously in ref. [2] for the  $\pi^0$  channel [55]. This fit used our data in the limited  $Q^2$ -range of [0.85, 1.15] GeV<sup>2</sup> instead of the present range [0.4, 2.2] GeV<sup>2</sup>, and it turned out that the obtained  $b$  values were usually smaller than the present ones. In the bin  $W \in [1.5, 1.6]$  GeV, this limited fit yielded  $b = 0.6 \pm 0.1$  GeV<sup>-2</sup>. The present global  $Q^2$  fit in the same  $W$ -bin yields  $b = 0.93 \pm 0.02$  GeV<sup>-2</sup>. This latter value better represents the average  $Q^2$ -evolution of the cross section, in the full  $Q^2$ -range [0.4, 2.2] GeV<sup>2</sup>.

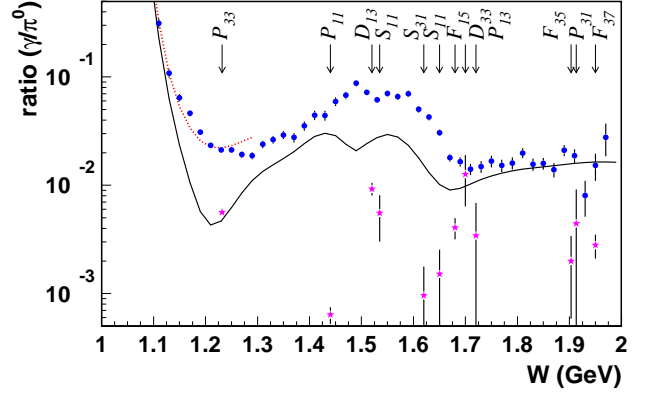


FIG. 7: (Color online) Ratio of the reduced cross sections ( $d^2\sigma$ ) of the processes  $H(e, e'p)\gamma$  and  $H(e, e'p)\pi^0$ , at  $Q^2 = 1$  GeV<sup>2</sup>,  $\cos\theta_{c.m.} = -0.975$  and  $k_{lab} = 4.032$  GeV (full circles; statistical error only). The full curve and the dotted curve for  $W < 1.3$  GeV are this ratio, at the same kinematics, calculated using different theoretical models (see text section III C). The stars represent the ratio  $r_{N^*}$  (see text section III C) for the listed individual resonances, as obtained from [29].

### C. VCS to $\pi^0$ Ratio

From the present results and those published in [2], we have determined the experimental ratio between the  $H(e, e'p)\gamma$  and  $H(e, e'p)\pi^0$  cross sections at  $\cos\theta_{\gamma}^* = -0.975$  and  $Q^2 = 1$  GeV<sup>2</sup> for the entire resonance region (see Table IX). In Fig. 7 we show the value of the ratio of the  $\phi$ -independent cross sections,  $r = \langle d^2\sigma_{\gamma} \rangle / \langle d^2\sigma_{\pi^0} \rangle$ . Two theoretical calculations of this observable are also displayed: the full curve is obtained with BH+Born+ $\pi^0$ -exchange for the  $H(e, e'p)\gamma$  reaction (numerator) and MAID2003 [23] for the  $H(e, e'p)\pi^0$  reaction (denominator); the dotted curve is obtained by changing the numerator to the DR model for VCS [17]. This latter calculation agrees well with our data in the  $\Delta(1232)$  resonance region. As a reference, we have also indicated (in star symbols) the value of the simple ratio of the branching ratios of the individual resonances [29]:  $r_{N^*} = BR(N^* \rightarrow p\gamma) / BR(N^* \rightarrow N\pi)$ . This ratio  $r_{N^*}$  is integrated over  $4\pi$  in the final state, therefore it has different dynamical sensitivity than our backward data and should not be directly compared to them. Furthermore, there are important interference effects between individual resonances, at the amplitude level, which are not considered in  $r_{N^*}$ , while they are -at least partially- taken into account in the theoretical curves of Fig. 7.

Below the  $\Delta(1232)$  resonance, the large enhancement of the ratio is due to the rising (BH+B) cross section in the VCS channel. We note the large enhancement of the measured ratio also in the second resonance region ( $P_{11}$ ,  $D_{13}$ ,  $S_{11}$ ). These particular resonances have large couplings to the  $N\pi\pi$  and  $N\eta$  channels, which contribute as virtual channels to the VCS process. We have already

noted the likely significance of these resonances for the Generalized Polarizabilities. The observed variation of the ratio  $r$  with  $W$  illustrates our initial motivation: the VCS and  $\gamma^*p \rightarrow \pi^0 p$  channels have very different sensitivities to the resonances.

#### D. VCS-RCS Comparison

The RCS reaction  $\gamma p \rightarrow \gamma p$  has been intensively investigated in the  $\Delta(1232)$ -resonance [30] and in the high-energy diffractive region [31]. It was also studied above the  $\Delta(1232)$  at Bonn [32], Saskatoon [33], and Tokyo [34, 35]. The Cornell experiment [36] measured the RCS process at photon energies  $E_\gamma$  in the range 2–6 GeV and angles from  $45^\circ$  to  $128^\circ$  in the c.m. frame. There are no high-energy fully backward RCS data. The recent JLab experiment E99-114 [37, 38] measured the RCS process at  $E_\gamma$  in the range 3–6 GeV. The large-angle data at fixed  $W$  are roughly independent of  $\theta_{c.m.}$  (within a factor of two) in the range  $[90^\circ, 120^\circ]$  [38].

In Fig. 8 we compare our VCS data at backward angle with existing large-angle RCS data. For this purpose we have used the VCS reduced cross section defined in section III B, determined in the experimental scan at fixed  $Q^2 = 1 \text{ GeV}^2$  and  $\cos \theta_{\gamma\gamma}^* = -0.975$ , and the data have been converted in terms of  $d\sigma/dt$  (see Table IX). In this figure, at low  $W$ , we see again the rapid rise in the VCS cross section due to the coherent sum of the BH and Born amplitudes. As illustrated previously in Fig. 3, the VCS excitation in the  $\Delta(1232)$  region is accurately fitted by the Dispersion Relations, including both the onshell  $N \rightarrow \Delta$  transition form factors and the Generalized Polarizabilities [1]. Above the  $\Delta$ -resonance we do not have an explicit model of the VCS process. Through the second resonance region ( $W \approx 1600 \text{ MeV}$ ) the RCS and VCS data show on-shell  $s$ -channel resonances. The VCS/RCS comparison in this region shows a strong decrease of the cross section from  $Q^2 = 0$  to  $Q^2 = 1 \text{ GeV}^2$ , as expected from  $s$ -channel resonance form factors.

The VCS/RCS comparison for  $W \geq 1.8 \text{ GeV}$  is in marked contrast with the behavior at lower  $W$ . At high  $W$  the VCS cross section intercepts the trend of the largest-angle RCS cross sections ( $\theta_{c.m.} \approx 130^\circ$ ), around  $W = 2 \text{ GeV}$ . Also, for  $W > 2 \text{ GeV}$  the  $W^{-2n}$ -scaling of the RCS data has a completely different trend than the (BH+Born+ $\pi^0$ -exchange) VCS curve, which seems to form a baseline for the VCS data at lower  $W$ .

We briefly review the high-energy behavior of the Compton amplitude in three kinematic domains:  $-t \ll W^2$  (forward Compton scattering);  $-t \approx W^2/2$  (wide-angle Compton scattering), and the present domain of  $-t \approx W^2$  (backward Compton scattering).

- Forward Compton scattering at high energy and at  $Q^2 = 0$  (RCS) can be described by  $t$ -channel Regge exchange processes [31]. As the photon virtuality increases, the Regge exchange amplitudes are suppressed by factors of  $m_V^2/(m_V^2 + Q^2)$  from the

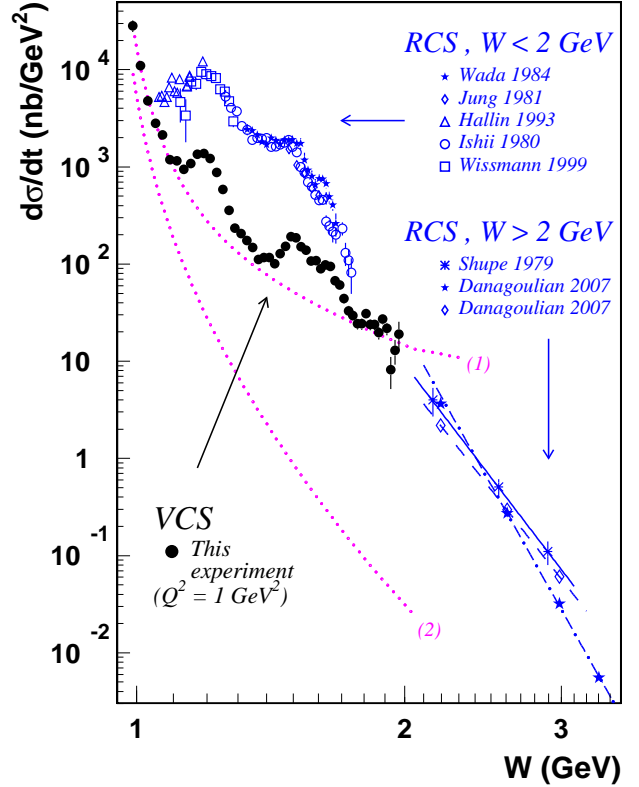


FIG. 8: (Color online) Comparison of VCS data from this experiment ( $\bullet$ ) at ( $Q^2 = 1 \text{ GeV}^2$ ,  $\theta_{\gamma\gamma}^* = 167.2^\circ$ ) and RCS data, for  $W < 2 \text{ GeV}$  at  $\theta_{c.m.} = 159 - 162^\circ$  ( $\star$ ) [34],  $\theta_{c.m.} = 128 - 132^\circ$  ( $\diamond$ ) [32],  $\theta_{c.m.} = 141^\circ$  ( $\triangle$ ) [33],  $\theta_{c.m.} = 130 - 133^\circ$  ( $\circ$ ) [39] and  $\theta_{c.m.} = 131^\circ$  ( $\square$ ) [30], and for  $W > 2 \text{ GeV}$  at  $\theta_{c.m.} = 105 - 128^\circ$  ( $\ast$ ) [36],  $\theta_{c.m.} = 113^\circ$  ( $\star$ ) and  $128^\circ$  ( $\diamond$ ) [38]. The dotted curves labelled (1) and (2) are the BH+Born+ $\pi^0$ -exchange cross section (see text) and the BH one, respectively. For  $W > 2 \text{ GeV}$ , the solid curve is an  $s^{-6}$  power law normalized to the  $W = 2.55 \text{ GeV}$  Cornell point of ref. [36], the dot-dashed and dashed curves are  $s^{-8.1}$  and  $s^{-5.3}$  power laws fitted to the JLab data [38] at  $\theta_{c.m.} = 113^\circ$  and  $128^\circ$ , respectively.

vector meson poles (of mass  $m_V$ ) in the entrance channel. At high  $Q^2$  (but empirically only several  $\text{GeV}^2$ ) the forward Compton amplitude is dominated by the perturbative, leading-twist "handbag" amplitude of Deep Inelastic Scattering (DIS) [29]. Similarly, a recent QCD factorization theorem [40, 41] predicts that in the off-forward deeply virtual limit ( $-t/Q^2 \ll 1$ ), the DVCS  $\gamma^*p \rightarrow p\gamma$  amplitude factorizes the perturbative  $\gamma^*q \rightarrow q\gamma$  amplitude on an elementary quark in the target, convoluted with twist-2 quark (or gluon, at low Bjorken scaling variable  $x_B$ ) matrix elements called Generalized Parton Distributions (GPDs). Recent DVCS experiments have found evidence for the perturbative mechanism at  $Q^2$ -scales of several  $\text{GeV}^2$  [42, 43, 44, 45, 46];



- Wide-angle Compton scattering at sufficiently high energies will be dominated by the perturbative two-gluon exchange kernel [47]. The presently available RCS data with  $(W^2, -t, M^2 - u)$  all being large [36, 37, 38] are consistent with a sub-asymptotic model based on the elementary Klein-Nishina (or “ $\gamma q \rightarrow q\gamma$  handbag”) process on a single quark, convoluted with high-momentum configurations in the proton [48, 49, 50];
- We expect that the high-energy RCS amplitude at  $\theta_{\text{c.m.}} \approx \pi$  is dominated by  $u$ -channel Regge exchange. This  $u$ -channel Regge behavior is seen, for example in the  $\gamma p \rightarrow n\pi^+$  reaction in the backward direction [51]. On the other hand, as  $Q^2$  increases it is likely that the Regge exchange mechanism is strongly suppressed in the backward direction (just as it is for forward Compton scattering), and thus we do not expect it to be dominant in our VCS kinematics. In RCS, only at high transverse momentum  $p_T$ , corresponding to both  $-t$  and  $M^2 - u$  being large, is the perturbative mechanism expected to be dominant. Inspired by the  $Q^2$ -scaling behavior in DIS and DVCS, we may suggest that, as  $W^2$  and  $Q^2$  increase, in the backward VCS cross section there is a transition to a hard-scattering process at the quark level. Of course more VCS data at high  $W$  ( $\geq 2$  GeV) and backward angles would be needed in order to explore this conjecture.

A QCD description of VCS in the backward region has been proposed [52]. This is a different kind of factorization relative to DVCS in the forward region. In the forward kinematics, the hard subprocess is the exchange of two partons (the handbag diagram) and the GPDs encode the hadronic part of the amplitude. In the backward kinematics, the hard subprocess is the exchange of three quarks, and  $N \rightarrow qq\bar{q}\gamma$  transition distribution amplitudes (TDAs) replace the GPDs. This picture should be valid at large enough values of  $Q^2$  and  $W^2$ , and must be tested independently in each channel (*e.g.* backward VCS,  $p\bar{p} \rightarrow \gamma^*\gamma\dots$ ). In particular, the matrix element of the  $\gamma^*p \rightarrow \gamma p$  scattering amplitude is predicted to have the following asymptotics in the backward direction at fixed  $x_B = Q^2/(W^2 - M^2 + Q^2)$  (**not** fixed  $W^2$ ) [53, 54]:

$$\mathcal{M} \sim \frac{\alpha_S^2(Q^2)}{Q^3} \quad (3)$$

where  $\alpha_S$  is the strong coupling constant. Neglecting terms of order  $M^2/W^2$ , this scaling law is obtained for  $Q^2/W^2$  fixed. Following the Hand convention [20] utilized in [54], the  $\gamma^*p \rightarrow \gamma p$  differential cross section will have the following scaling:

$$\frac{d\sigma}{dt} = \frac{1}{16\pi(W^2 - M^2)^2} |\mathcal{M}|^2 \quad (4)$$

$$\sim \frac{\alpha_S^4(Q^2)}{(W^2)^5} \times f\left(\frac{Q^2}{W^2}, u\right). \quad (5)$$

This asymptotic scaling law of  $W^{-10}$  predicted for backward VCS at fixed  $(Q^2/W^2, u)$  is different from the  $W^{-12}$  scaling predicted for wide-angle RCS at fixed  $-t/W^2$  [47]. A second scaling law applies to backward electroproduction, that the ratio of pion electroproduction to photon electroproduction should be  $Q^2$ -independent at large  $W^2$  and fixed  $x_B$  [53]:

$$\frac{d\sigma(\gamma^*p \rightarrow \gamma p)}{d\sigma(\gamma^*p \rightarrow \pi^0 p)} \sim (Q^2)^0 \quad \text{for } \theta_{\text{c.m.}} \approx \pi. \quad (6)$$

With the advent of the 12 GeV upgrade to JLab, it will be feasible to extend both RCS, VCS, and pion electroproduction measurements to higher  $W^2$  and higher  $Q^2$ . These data can establish empirically the scaling laws of the Compton amplitude in these new kinematic domains.

#### IV. CONCLUSION

In summary, the JLab experiment E93-050 studied for the first time the  $H(e, e'p)\gamma$  process in the nucleon resonance region. This experiment provides a dataset of cross sections that is unique at backward angles. For  $W \geq 1.4$  GeV, the BH contribution to photon electroproduction is small, and the reaction is dominated by the VCS process. The  $W$ -dependence of the VCS cross section shows resonance phenomena, as observed in RCS. Our data allow to compare the sensitivity to the various nucleon resonances in two different exit channels,  $\gamma p$  and  $\pi^0 p$ , namely by studying the  $Q^2$ -dependence of the cross section for the two reactions  $H(e, e'p)\gamma$  and  $H(e, e'p)\pi^0$ . The  $\gamma$ -to- $\pi^0$  ratio shows strong variations with  $W$  across the resonance region. At our highest  $W$  (1.8-1.9 GeV) the comparison with wide-angle RCS may suggest that the VCS process undergoes a transition to a hard-scattering mechanism at the quark level. Therefore the data presented in this paper emphasize the interest of exploring a new kinematic domain of exclusive electroproduction reactions (high  $W$ , high  $Q^2$ , backward angles) in which new conjectures involving the fundamental degrees of freedom of QCD could be tested.

#### Acknowledgments

We would like to thank B.Pire for discussions, and B.Pasquini and M.Vanderhaeghen for providing their codes (regarding Dispersion Relations and radiative corrections, respectively).

We wish to acknowledge essential work of the JLab accelerator staff and Hall A technical staff. This work was supported by DOE contract DE-AC05-84ER40150 under which the Southeastern Universities Research Association (SURA) operated the Thomas Jefferson National Accelerator Facility. We acknowledge additional grants from the US DOE and NSF, the French Centre

National de la Recherche Scientifique and Commissariat à l’Energie Atomique, the Conseil Régional d’Auvergne,

the FWO-Flanders (Belgium) and the BOF-Gent University.

- 
- [1] G. Laveissière *et al.* (Jefferson Lab Hall A), *Phys. Rev. Lett.* **93**, 122001 (2004).
- [2] G. Laveissière *et al.*, *Phys. Rev.* **C69**, 045203 (2004).
- [3] N. Isgur and G. Karl, *Phys. Rev.* **D19**, 2653 (1979).
- [4] R. Koniuk and N. Isgur, *Phys. Rev. Lett.* **44**, 845 (1980).
- [5] I. Niculescu *et al.*, *Phys. Rev. Lett.* **85**, 1186 (2000).
- [6] J. Roche *et al.*, *Phys. Rev. Lett.* **85**, 708 (2000).
- [7] P. Bourgeois *et al.*, *Phys. Rev. Lett.* **97**, 212001 (2006).
- [8] P. Janssens *et al.* (MAMI-A1), *Eur. Phys. J.* **A37**, 1 (2008).
- [9] I. K. Bensafa *et al.* (MAMI-A1), *Eur. Phys. J.* **A32**, 69 (2007).
- [10] N. F. Sparveris *et al.*, *Phys. Rev.* **C78**, 018201 (2008).
- [11] H. Bethe and W. Heitler, *Proc. Roy. Soc. Lond.* **A146**, 83 (1934).
- [12] J. Alcorn *et al.*, *Nucl. Instrum. Meth.* **A522**, 294 (2004).
- [13] P. Janssens *et al.*, *Nucl. Instr. Meth.* **A566**, 675 (2006).
- [14] G. Laveissière, Ph.D. thesis, Université Blaise Pascal, Clermont-Fd, France (2001), DU 1309.
- [15] E. J. Brash, A. Kozlov, S. Li, and G. M. Huber, *Phys. Rev.* **C65**, 051001 (2002).
- [16] M. Vanderhaeghen, *Phys. Lett.* **B368**, 13 (1996).
- [17] B. Pasquini, M. Gorchtein, D. Drechsel, A. Metz, and M. Vanderhaeghen, *Eur. Phys. J.* **A11**, 185 (2001).
- [18] C. E. Hyde-Wright and K. de Jager, *Ann. Rev. Nucl. Part. Sci.* **54**, 217 (2004).
- [19] S. Capstick and B. D. Keister, *Phys. Rev.* **D47**, 860 (1993), and *Phys. Rev.* **D46**, 84 (1992).
- [20] L. N. Hand, *Phys. Rev.* **129**, 1834 (1963).
- [21] P. Stoler, *Phys. Rept.* **226**, 103 (1993).
- [22] L. Tiator *et al.*, *Eur. Phys. J.* **A19**, 55 (2004), and references therein.
- [23] D. Drechsel, O. Hanstein, S. S. Kamalov, and L. Tiator, *Nucl. Phys.* **A645**, 145 (1999), URL [www.kph.uni-mainz.de/MAID/](http://www.kph.uni-mainz.de/MAID/).
- [24] R. Arndt, W. Briscoe, I. Strakovsky, and R. Workman (2003), in Proceedings of the NSTAR2002 Workshop, nucl-th/0301068.
- [25] R. A. Arndt, W. J. Briscoe, I. I. Strakovsky, and R. L. Workman, *AIP Conf. Proc.* **904**, 269 (2007), nucl-th/0607017.
- [26] F. W. Brasse *et al.*, *Z. Phys.* **C22**, 33 (1984).
- [27] C. S. Armstrong *et al.* (Jefferson Lab E94014), *Phys. Rev.* **D60**, 052004 (1999).
- [28] H. Denizli *et al.* (CLAS), *Phys. Rev.* **C76**, 015204 (2007).
- [29] W. M. Yao *et al.* (Particle Data Group), *J. Phys.* **G33**, 1 (2006).
- [30] F. Wissmann *et al.*, *Nucl. Phys.* **A660**, 232 (1999).
- [31] T. H. Bauer, R. D. Spital, D. R. Yennie, and F. M. Pipkin, *Rev. Mod. Phys.* **50**, 261 (1978).
- [32] M. Jung *et al.*, *Zeit. Phys.* **C10**, 197 (1981).
- [33] E. L. Hallin *et al.*, *Phys. Rev.* **C48**, 1497 (1993).
- [34] Y. Wada *et al.*, *Nucl. Phys.* **B247**, 313 (1984).
- [35] T. Ishii *et al.*, *Nucl. Phys.* **B254**, 458 (1985).
- [36] M. A. Shupe *et al.*, *Phys. Rev.* **D19**, 1921 (1979).
- [37] D. J. Hamilton *et al.* (Jefferson Lab Hall A), *Phys. Rev. Lett.* **94**, 242001 (2005).
- [38] A. Danagoulian *et al.* (Hall A), *Phys. Rev. Lett.* **98**, 152001 (2007).
- [39] T. Ishii *et al.*, *Nucl. Phys.* **B165**, 189 (1980).
- [40] X.-D. Ji and J. Osborne, *Phys. Rev.* **D58**, 094018 (1998).
- [41] J. C. Collins and A. Freund, *Phys. Rev.* **D59**, 074009 (1999).
- [42] C. Munoz Camacho *et al.* (Jefferson Lab Hall A), *Phys. Rev. Lett.* **97**, 262002 (2006).
- [43] F. X. Girod *et al.* (CLAS), *Phys. Rev. Lett.* **100**, 162002 (2008).
- [44] A. Airapetian *et al.* (HERMES), *Phys. Rev. Lett.* **87**, 182001 (2001).
- [45] F. D. Aaron *et al.* (H1), *Phys. Lett.* **B659**, 796 (2008).
- [46] S. Chekanov *et al.* (ZEUS), *Phys. Lett.* **B573**, 46 (2003).
- [47] S. J. Brodsky and G. R. Farrar, *Phys. Rev.* **D11**, 1309 (1975).
- [48] A. V. Radyushkin, *Phys. Rev.* **D58**, 114008 (1998).
- [49] H. W. Huang, P. Kroll, and T. Morii, *Eur. Phys. J.* **C23**, 301 (2002).
- [50] G. A. Miller, *Phys. Rev.* **C69**, 052201 (2004).
- [51] M. Guidal, J. M. Laget, and M. Vanderhaeghen, *Phys. Lett.* **B400**, 6 (1997).
- [52] B. Pire and L. Szymanowski, *Phys. Rev.* **D71**, 111501 (2005).
- [53] J. P. Lansberg, B. Pire, and L. Szymanowski, *Nucl. Phys.* **A782**, 16 (2007).
- [54] J. P. Lansberg, B. Pire, and L. Szymanowski, *Phys. Rev.* **D75**, 074004 (2007).
- [55] In ref. [2], eq.(17) has a misprint. The exponential fit should read  $e^{+b_{exp}(1\text{GeV}^2-Q^2)}$ .

## APPENDIX A: CROSS SECTION TABLES

This Appendix lists in detail the experimental cross section corresponding to the different studies presented in the paper. All cross sections are determined at a fixed incoming electron energy of 4.032 GeV. Ascii files of the tables are available at URL:

<http://clrwww.in2p3.fr/sondem/E93050-tables-RES/>  
or upon request to the authors. Due to the choice of method [13], the cross section is determined at well-defined points in phase space. These kinematic values have no error, and the uncertainty is entirely reported on the cross section. Error bars are given as r.m.s.

Tables I, II, III correspond to the study of section III A. They contain the  $H(e, e'p)\gamma$  five-fold differential cross section  $d^5\sigma/(dk'_{lab} d[\Omega_e]_{lab} d[\Omega_p]_{c.m.})$  at fixed  $Q^2 = 1 \text{ GeV}^2$ , for  $\cos\theta_{\gamma}^* = -0.975, -0.875$  and  $-0.650$  respectively, and six values of  $\phi$ . A bin is empty if the number of events is smaller than 5, or the systematic error very large ( $> 1.5 \times d^5\sigma$ ).

Tables IV to VII correspond to the study of section III B. They give the measured cross section in the most elementary bins, covering the  $Q^2$ -range [0.43,

2.15] GeV<sup>2</sup>, the  $W$ -range [1.45, 1.59] GeV, at fixed  $\cos\theta_{\gamma\gamma}^*$  or  $\cos\theta_{c.m.} = -0.975$  and for six bins in  $\phi$ . Tables IV and V give the five-fold cross section  $d^5\sigma/(dk'_{lab} d[\Omega_e]_{lab} d[\Omega_p]_{c.m.})$  for the  $H(e, e'p)\gamma$  process, while tables VI and VII give the two-fold cross section  $d^2\sigma/d[\Omega_p]_{c.m.}$  of Eq. 1 for the  $H(e, e'p)\pi^0$  process. A bin is empty if the number of events is smaller than 2.

Table VIII contains the data depicted in Figs. 4 and 5. As explained in the text, for the  $H(e, e'p)\gamma$  process this cross section  $\langle d^2\sigma_\gamma \rangle$  is obtained from the raw data of Tables IV and V, by dividing by the virtual photon flux, performing a (model-based)  $\phi$ -analysis, keeping only the  $\phi$ -independent term and then grouping three elementary bins in  $W$  (at 1.51, 1.53 and 1.55 GeV). For the  $H(e, e'p)\pi^0$  process this cross section  $\langle d^2\sigma_{\pi^0} \rangle$  is obtained from the raw data of Table VII at  $W = 1.53$  GeV, by

performing only the  $\phi$ -analysis step.

Table IX gives the ratio  $r = \langle d^2\sigma_\gamma \rangle / \langle d^2\sigma_{\pi^0} \rangle$  depicted in Fig. 7. This table also provides the values of the reduced cross section in the photon electroproduction channel corresponding to Fig. 8. Note that in VCS, the conversion from  $d^2\sigma/d[\Omega_p]_{c.m.}$  to  $d\sigma/dt$  is the following:

$$\frac{d^2\sigma}{d[\Omega_p]_{c.m.}} = \frac{d\sigma}{dt} \cdot J \quad , \quad \text{with:}$$

$$J = \frac{1}{2\pi} \cdot \frac{(s - M_p^2) \cdot [4Q^2s + (s - M_p^2 - Q^2)^2]^{\frac{1}{2}}}{2s}$$

where  $s$  and  $t$  are the Mandelstam variables defined in section IA.

TABLE I:  $H(e, e'p)\gamma$  cross section  $d^5\sigma/(dk'_{lab} d[\Omega_e]_{lab} d[\Omega_p]_{c.m.})$  ( $\pm$  statistical  $\pm$  systematic error) at  $Q^2=1.0$  GeV<sup>2</sup> and  $\cos\theta_{\gamma\gamma}^* = -0.975$ , in fb/(MeV  $\cdot$  sr<sup>2</sup>).

$W$ (GeV)	$\phi = 15^\circ$	$\phi = 45^\circ$	$\phi = 75^\circ$	$\phi = 105^\circ$	$\phi = 135^\circ$	$\phi = 165^\circ$
0.99			231 $\pm$ 84 $\pm$ 101	200 $\pm$ 70 $\pm$ 77	243 $\pm$ 59 $\pm$ 108	288 $\pm$ 59 $\pm$ 104
1.01	14.9 $\pm$ 5.4 $\pm$ 5.6	60 $\pm$ 32 $\pm$ 36	111 $\pm$ 30 $\pm$ 20	161 $\pm$ 33 $\pm$ 30	188 $\pm$ 34 $\pm$ 64	254 $\pm$ 36 $\pm$ 45
1.03	8.1 $\pm$ 4.1 $\pm$ 4.3	45 $\pm$ 14 $\pm$ 6	85 $\pm$ 21 $\pm$ 14	119 $\pm$ 22 $\pm$ 24	134 $\pm$ 22 $\pm$ 20	152 $\pm$ 22 $\pm$ 33
1.05	28.4 $\pm$ 8.3 $\pm$ 4.7	41 $\pm$ 13 $\pm$ 15	77 $\pm$ 17 $\pm$ 23	114 $\pm$ 19 $\pm$ 23	114 $\pm$ 19 $\pm$ 15	83 $\pm$ 15 $\pm$ 62
1.07	14.6 $\pm$ 6.8 $\pm$ 4.0	57 $\pm$ 14 $\pm$ 9	59 $\pm$ 13 $\pm$ 13	104 $\pm$ 17 $\pm$ 18	94 $\pm$ 15 $\pm$ 25	128 $\pm$ 18 $\pm$ 24
1.09	29 $\pm$ 10 $\pm$ 4	39 $\pm$ 11 $\pm$ 10	71 $\pm$ 14 $\pm$ 9	68 $\pm$ 12 $\pm$ 10	63 $\pm$ 11 $\pm$ 12	67 $\pm$ 12 $\pm$ 24
1.11	14.4 $\pm$ 6.4 $\pm$ 5.0	34 $\pm$ 10 $\pm$ 2	66 $\pm$ 12 $\pm$ 9	97 $\pm$ 14 $\pm$ 11	109 $\pm$ 16 $\pm$ 9	71 $\pm$ 13 $\pm$ 18
1.13	36 $\pm$ 11 $\pm$ 7	46 $\pm$ 10 $\pm$ 7	59 $\pm$ 11 $\pm$ 15	75 $\pm$ 13 $\pm$ 8	82 $\pm$ 15 $\pm$ 17	69 $\pm$ 15 $\pm$ 3
1.15	30 $\pm$ 9 $\pm$ 15	82 $\pm$ 14 $\pm$ 15	95 $\pm$ 15 $\pm$ 9	79 $\pm$ 14 $\pm$ 14	125 $\pm$ 20 $\pm$ 43	105 $\pm$ 18 $\pm$ 27
1.17	54 $\pm$ 12 $\pm$ 9	103 $\pm$ 16 $\pm$ 8	104 $\pm$ 17 $\pm$ 12	124 $\pm$ 17 $\pm$ 9	180 $\pm$ 22 $\pm$ 24	168 $\pm$ 22 $\pm$ 10
1.19	94 $\pm$ 16 $\pm$ 7	118 $\pm$ 17 $\pm$ 13	135 $\pm$ 17 $\pm$ 13	154 $\pm$ 18 $\pm$ 23	145 $\pm$ 19 $\pm$ 14	178 $\pm$ 24 $\pm$ 15
1.21	119 $\pm$ 18 $\pm$ 17	117 $\pm$ 17 $\pm$ 20	167 $\pm$ 18 $\pm$ 9	119 $\pm$ 15 $\pm$ 10	153 $\pm$ 21 $\pm$ 6	144 $\pm$ 24 $\pm$ 20
1.23	111 $\pm$ 16 $\pm$ 13	108 $\pm$ 15 $\pm$ 18	102 $\pm$ 13 $\pm$ 11	141 $\pm$ 16 $\pm$ 8	107 $\pm$ 17 $\pm$ 18	83 $\pm$ 15 $\pm$ 14
1.25	51 $\pm$ 11 $\pm$ 12	78 $\pm$ 12 $\pm$ 11	94 $\pm$ 12 $\pm$ 11	74 $\pm$ 13 $\pm$ 10	81 $\pm$ 11 $\pm$ 6	96 $\pm$ 12 $\pm$ 10
1.27	41.3 $\pm$ 9.2 $\pm$ 7.1	51.5 $\pm$ 9.3 $\pm$ 6.3	48.1 $\pm$ 9.8 $\pm$ 6.9	64.4 $\pm$ 9.5 $\pm$ 4.1	61.4 $\pm$ 8.3 $\pm$ 4.8	47.1 $\pm$ 8.0 $\pm$ 5.9
1.29	45.2 $\pm$ 7.9 $\pm$ 4.5	40.3 $\pm$ 7.6 $\pm$ 7.1	42.1 $\pm$ 7.6 $\pm$ 3.6	40.1 $\pm$ 5.5 $\pm$ 3.9	43.0 $\pm$ 6.4 $\pm$ 3.6	35.0 $\pm$ 8.2 $\pm$ 5.0
1.31	29 $\pm$ 7 $\pm$ 15	18.0 $\pm$ 5.9 $\pm$ 5.4	42.3 $\pm$ 6.0 $\pm$ 2.4	37.0 $\pm$ 5.0 $\pm$ 3.1	41.4 $\pm$ 7.7 $\pm$ 3.5	43 $\pm$ 11 $\pm$ 7
1.33	41 $\pm$ 8 $\pm$ 10	33.0 $\pm$ 6.1 $\pm$ 3.1	39.7 $\pm$ 4.8 $\pm$ 3.2	31.1 $\pm$ 5.1 $\pm$ 3.4	28.8 $\pm$ 8.0 $\pm$ 6.5	20.9 $\pm$ 8.6 $\pm$ 1.4
1.35	19.9 $\pm$ 4.8 $\pm$ 4.4	21.2 $\pm$ 4.2 $\pm$ 4.4	30.2 $\pm$ 4.0 $\pm$ 2.1	35.1 $\pm$ 6.6 $\pm$ 6.7	27.1 $\pm$ 8.3 $\pm$ 8.0	23.9 $\pm$ 8.8 $\pm$ 5.4
1.37	17.5 $\pm$ 4.1 $\pm$ 4.3	21.6 $\pm$ 3.7 $\pm$ 2.1	30.5 $\pm$ 4.6 $\pm$ 2.4	11.8 $\pm$ 5.0 $\pm$ 9.5	24.4 $\pm$ 7.3 $\pm$ 2.1	22.5 $\pm$ 9.6 $\pm$ 8.2
1.39	18.0 $\pm$ 3.8 $\pm$ 3.1	24.2 $\pm$ 3.9 $\pm$ 4.0	18.5 $\pm$ 4.7 $\pm$ 4.4	23.5 $\pm$ 5.8 $\pm$ 4.8	29.1 $\pm$ 8.5 $\pm$ 6.8	33 $\pm$ 11 $\pm$ 3
1.41	23.0 $\pm$ 4.3 $\pm$ 1.3	20.3 $\pm$ 4.2 $\pm$ 2.0	19.8 $\pm$ 5.1 $\pm$ 4.8	31.8 $\pm$ 6.2 $\pm$ 5.1	24.7 $\pm$ 7.8 $\pm$ 3.6	32 $\pm$ 10 $\pm$ 4
1.43	23.9 $\pm$ 4.8 $\pm$ 2.3	20.8 $\pm$ 5.0 $\pm$ 5.3	16.8 $\pm$ 4.5 $\pm$ 3.0	21.6 $\pm$ 5.6 $\pm$ 2.4	33.7 $\pm$ 8.0 $\pm$ 4.7	27.0 $\pm$ 8.5 $\pm$ 5.5
1.45	15.6 $\pm$ 4.9 $\pm$ 4.1	24.8 $\pm$ 6.1 $\pm$ 3.2	30.8 $\pm$ 5.8 $\pm$ 2.2	33.4 $\pm$ 6.6 $\pm$ 4.5	36.7 $\pm$ 7.3 $\pm$ 5.1	45 $\pm$ 10 $\pm$ 6
1.47	34.3 $\pm$ 7.4 $\pm$ 2.9	33.8 $\pm$ 6.5 $\pm$ 3.6	37.0 $\pm$ 6.2 $\pm$ 2.3	37.5 $\pm$ 6.0 $\pm$ 4.9	44.8 $\pm$ 8.0 $\pm$ 6.0	39 $\pm$ 10 $\pm$ 4
1.49	41.5 $\pm$ 7.8 $\pm$ 4.0	41.5 $\pm$ 6.8 $\pm$ 4.2	45.5 $\pm$ 6.3 $\pm$ 8.8	45.4 $\pm$ 5.9 $\pm$ 7.0	64 $\pm$ 9 $\pm$ 10	67 $\pm$ 11 $\pm$ 10
1.51	36.5 $\pm$ 6.7 $\pm$ 4.6	36.6 $\pm$ 6.1 $\pm$ 4.0	48.6 $\pm$ 5.6 $\pm$ 5.9	50.8 $\pm$ 6.1 $\pm$ 5.8	47.6 $\pm$ 7.4 $\pm$ 5.2	85 $\pm$ 11 $\pm$ 11
1.53	39.8 $\pm$ 6.7 $\pm$ 4.7	39.9 $\pm$ 6.0 $\pm$ 5.4	37.0 $\pm$ 4.9 $\pm$ 4.6	42.4 $\pm$ 5.6 $\pm$ 4.5	39.9 $\pm$ 6.2 $\pm$ 3.7	50.4 $\pm$ 8.7 $\pm$ 6.3
1.55	37.1 $\pm$ 6.3 $\pm$ 2.5	31.4 $\pm$ 4.8 $\pm$ 3.9	26.8 $\pm$ 4.0 $\pm$ 4.6	39.0 $\pm$ 4.9 $\pm$ 3.6	57.8 $\pm$ 7.0 $\pm$ 5.2	61 $\pm$ 10 $\pm$ 7
1.57	15.6 $\pm$ 3.9 $\pm$ 3.8	19.7 $\pm$ 3.8 $\pm$ 3.5	32.7 $\pm$ 4.1 $\pm$ 2.8	36.8 $\pm$ 4.3 $\pm$ 3.2	41.3 $\pm$ 6.9 $\pm$ 7.3	31 $\pm$ 9 $\pm$ 10
1.59	18.5 $\pm$ 3.9 $\pm$ 1.3	30.0 $\pm$ 4.2 $\pm$ 3.1	31.5 $\pm$ 3.8 $\pm$ 3.5	40.1 $\pm$ 4.7 $\pm$ 4.7	27.8 $\pm$ 6.4 $\pm$ 5.0	26.0 $\pm$ 7.2 $\pm$ 8.9
1.61	18.1 $\pm$ 3.7 $\pm$ 3.4	21.7 $\pm$ 3.7 $\pm$ 3.5	28.9 $\pm$ 3.5 $\pm$ 3.7	23.8 $\pm$ 4.5 $\pm$ 3.5	31.8 $\pm$ 5.9 $\pm$ 2.4	26.2 $\pm$ 6.4 $\pm$ 4.0
1.63	19.0 $\pm$ 4.0 $\pm$ 2.2	26.4 $\pm$ 3.8 $\pm$ 1.8	29.4 $\pm$ 3.8 $\pm$ 2.6	27.0 $\pm$ 4.4 $\pm$ 4.3	32.6 $\pm$ 5.2 $\pm$ 4.2	35.8 $\pm$ 6.7 $\pm$ 2.7
1.65	20.4 $\pm$ 4.1 $\pm$ 3.3	25.1 $\pm$ 3.7 $\pm$ 2.2	22.3 $\pm$ 3.6 $\pm$ 3.8	29.2 $\pm$ 3.8 $\pm$ 2.4	39.5 $\pm$ 5.6 $\pm$ 5.0	36.8 $\pm$ 7.5 $\pm$ 6.8
1.67	17.7 $\pm$ 3.6 $\pm$ 3.4	16.2 $\pm$ 3.2 $\pm$ 1.6	26.1 $\pm$ 3.5 $\pm$ 2.2	18.8 $\pm$ 3.1 $\pm$ 2.4	17.0 $\pm$ 5.3 $\pm$ 4.7	19.7 $\pm$ 8.3 $\pm$ 3.2
1.69	10.8 $\pm$ 3.2 $\pm$ 2.6	16.2 $\pm$ 3.4 $\pm$ 3.6	21.5 $\pm$ 3.0 $\pm$ 4.5	16.0 $\pm$ 3.6 $\pm$ 2.9	31 $\pm$ 13 $\pm$ 26	22 $\pm$ 14 $\pm$ 9
1.71	13.1 $\pm$ 3.7 $\pm$ 3.8	13.3 $\pm$ 3.1 $\pm$ 1.5	14.1 $\pm$ 2.6 $\pm$ 3.5	8.9 $\pm$ 4.3 $\pm$ 1.9	16.8 $\pm$ 5.6 $\pm$ 2.3	9.5 $\pm$ 5.0 $\pm$ 2.5
1.73	3.4 $\pm$ 2.4 $\pm$ 3.0	6.2 $\pm$ 2.4 $\pm$ 4.5	8.4 $\pm$ 2.8 $\pm$ 2.0	14.4 $\pm$ 3.6 $\pm$ 2.0	16.7 $\pm$ 3.4 $\pm$ 3.4	14.3 $\pm$ 3.7 $\pm$ 2.3
1.75	17.2 $\pm$ 3.5 $\pm$ 2.0	6.5 $\pm$ 2.5 $\pm$ 1.9	11.1 $\pm$ 3.3 $\pm$ 1.3	10.3 $\pm$ 2.2 $\pm$ 2.6	6.7 $\pm$ 2.4 $\pm$ 1.3	8.2 $\pm$ 3.0 $\pm$ 1.4
1.77	4.2 $\pm$ 2.9 $\pm$ 5.4	5.1 $\pm$ 2.5 $\pm$ 0.9	7.1 $\pm$ 2.2 $\pm$ 1.7	8.0 $\pm$ 1.7 $\pm$ 1.0	8.0 $\pm$ 2.4 $\pm$ 2.3	11.6 $\pm$ 3.4 $\pm$ 1.6
1.79	5.6 $\pm$ 2.6 $\pm$ 3.3	9.6 $\pm$ 2.6 $\pm$ 1.8	7.0 $\pm$ 1.6 $\pm$ 1.8	8.4 $\pm$ 1.7 $\pm$ 0.8	3.7 $\pm$ 4.0 $\pm$ 3.5	4.6 $\pm$ 4.0 $\pm$ 3.5
1.81	4.9 $\pm$ 2.0 $\pm$ 2.0	8.8 $\pm$ 2.0 $\pm$ 0.9	7.9 $\pm$ 1.5 $\pm$ 0.8	13.6 $\pm$ 2.2 $\pm$ 3.1	19 $\pm$ 9 $\pm$ 10	18.6 $\pm$ 9.3 $\pm$ 9.8
1.83	8.2 $\pm$ 1.9 $\pm$ 1.1	5.7 $\pm$ 1.6 $\pm$ 1.1	7.7 $\pm$ 1.6 $\pm$ 0.9	5.6 $\pm$ 3.1 $\pm$ 5.1	4.9 $\pm$ 3.6 $\pm$ 2.1	7.1 $\pm$ 4.3 $\pm$ 2.8
1.85	4.6 $\pm$ 1.7 $\pm$ 0.9	8.4 $\pm$ 1.8 $\pm$ 1.5	5.6 $\pm$ 1.8 $\pm$ 1.7	7.3 $\pm$ 2.4 $\pm$ 1.1	9.2 $\pm$ 2.7 $\pm$ 1.0	8.3 $\pm$ 3.2 $\pm$ 2.2
1.87	4.6 $\pm$ 1.9 $\pm$ 1.2	4.8 $\pm$ 2.1 $\pm$ 1.2	5.4 $\pm$ 2.0 $\pm$ 1.6	6.4 $\pm$ 1.8 $\pm$ 0.8	7.1 $\pm$ 2.3 $\pm$ 2.3	6.6 $\pm$ 2.9 $\pm$ 1.4
1.89	11 $\pm$ 4 $\pm$ 11	8.7 $\pm$ 2.6 $\pm$ 2.2	8.2 $\pm$ 1.8 $\pm$ 0.9	5.8 $\pm$ 1.6 $\pm$ 1.0	13.5 $\pm$ 2.9 $\pm$ 2.8	7.8 $\pm$ 3.6 $\pm$ 1.9
1.91	10.1 $\pm$ 2.6 $\pm$ 1.9	4.2 $\pm$ 2.7 $\pm$ 1.8	5.0 $\pm$ 1.4 $\pm$ 1.2	7.3 $\pm$ 1.8 $\pm$ 1.8	5.7 $\pm$ 3.7 $\pm$ 1.8	10.0 $\pm$ 5.9 $\pm$ 3.9
1.93	1.4 $\pm$ 1.7 $\pm$ 1.9	1.5 $\pm$ 1.4 $\pm$ 1.8	3.2 $\pm$ 1.4 $\pm$ 1.2	2.5 $\pm$ 2.2 $\pm$ 1.8		
1.95	5.2 $\pm$ 1.8 $\pm$ 1.9	2.8 $\pm$ 1.5 $\pm$ 1.8	2.8 $\pm$ 1.7 $\pm$ 1.2			
1.97	3.3 $\pm$ 2.1 $\pm$ 1.9	6.4 $\pm$ 2.4 $\pm$ 1.8				

TABLE II:  $H(e, e'p)\gamma$  cross section  $d^5\sigma/(dk'_{lab} d[\Omega_e]_{lab} d[\Omega_p]_{c.m.})$  ( $\pm$  statistical  $\pm$  systematic error) at  $Q^2=1.0$  GeV<sup>2</sup> and  $\cos\theta_{\gamma^*} = -0.875$ , in fb/(MeV  $\cdot$  sr<sup>2</sup>).

$W$ (GeV)	$\phi = 15^\circ$	$\phi = 45^\circ$	$\phi = 75^\circ$	$\phi = 105^\circ$	$\phi = 135^\circ$	$\phi = 165^\circ$
0.99		548 $\pm$ 306 $\pm$ 112	362 $\pm$ 159 $\pm$ 75	459 $\pm$ 107 $\pm$ 63	453 $\pm$ 78 $\pm$ 46	478 $\pm$ 72 $\pm$ 39
1.01		230 $\pm$ 94 $\pm$ 94	320 $\pm$ 75 $\pm$ 54	342 $\pm$ 54 $\pm$ 30	361 $\pm$ 47 $\pm$ 42	291 $\pm$ 37 $\pm$ 28
1.03	65 $\pm$ 27 $\pm$ 14	186 $\pm$ 60 $\pm$ 26	263 $\pm$ 48 $\pm$ 33	224 $\pm$ 34 $\pm$ 17	280 $\pm$ 34 $\pm$ 20	283 $\pm$ 32 $\pm$ 22
1.05		144 $\pm$ 43 $\pm$ 13	204 $\pm$ 35 $\pm$ 23	197 $\pm$ 28 $\pm$ 14	144 $\pm$ 22 $\pm$ 18	141 $\pm$ 21 $\pm$ 11
1.07		124 $\pm$ 34 $\pm$ 18	87 $\pm$ 19 $\pm$ 9	154 $\pm$ 22 $\pm$ 12	134 $\pm$ 19 $\pm$ 6	157 $\pm$ 20 $\pm$ 14
1.09		115 $\pm$ 29 $\pm$ 10	143 $\pm$ 23 $\pm$ 9	96 $\pm$ 16 $\pm$ 40	124 $\pm$ 17 $\pm$ 14	121 $\pm$ 19 $\pm$ 11
1.11	30 $\pm$ 15 $\pm$ 7	69 $\pm$ 20 $\pm$ 4	106 $\pm$ 18 $\pm$ 8	134 $\pm$ 18 $\pm$ 10	129 $\pm$ 21 $\pm$ 13	81 $\pm$ 20 $\pm$ 45
1.13	30 $\pm$ 14 $\pm$ 5	85 $\pm$ 20 $\pm$ 8	82 $\pm$ 14 $\pm$ 6	114 $\pm$ 17 $\pm$ 4	78 $\pm$ 19 $\pm$ 16	105 $\pm$ 30 $\pm$ 11
1.15	59 $\pm$ 20 $\pm$ 3	45 $\pm$ 13 $\pm$ 12	133 $\pm$ 19 $\pm$ 9	99 $\pm$ 18 $\pm$ 18	98 $\pm$ 22 $\pm$ 13	116 $\pm$ 25 $\pm$ 10
1.17	31 $\pm$ 14 $\pm$ 8	43 $\pm$ 14 $\pm$ 15	110 $\pm$ 17 $\pm$ 5	107 $\pm$ 18 $\pm$ 11	118 $\pm$ 22 $\pm$ 14	106 $\pm$ 30 $\pm$ 14
1.19	130 $\pm$ 28 $\pm$ 26	118 $\pm$ 18 $\pm$ 8	123 $\pm$ 17 $\pm$ 11	126 $\pm$ 18 $\pm$ 12	145 $\pm$ 29 $\pm$ 18	272 $\pm$ 122 $\pm$ 90
1.21	103 $\pm$ 21 $\pm$ 11	124 $\pm$ 19 $\pm$ 7	135 $\pm$ 17 $\pm$ 5	183 $\pm$ 21 $\pm$ 11	177 $\pm$ 51 $\pm$ 18	217 $\pm$ 70 $\pm$ 46
1.23	129 $\pm$ 21 $\pm$ 8	117 $\pm$ 18 $\pm$ 6	135 $\pm$ 16 $\pm$ 9	133 $\pm$ 20 $\pm$ 12	130 $\pm$ 24 $\pm$ 42	68 $\pm$ 19 $\pm$ 28
1.25	99 $\pm$ 17 $\pm$ 6	95 $\pm$ 17 $\pm$ 6	99 $\pm$ 13 $\pm$ 7	68 $\pm$ 14 $\pm$ 8	88 $\pm$ 14 $\pm$ 14	81 $\pm$ 21 $\pm$ 8
1.27	54 $\pm$ 13 $\pm$ 7	61 $\pm$ 13 $\pm$ 14	87 $\pm$ 13 $\pm$ 5	71 $\pm$ 11 $\pm$ 6	58 $\pm$ 12 $\pm$ 7	
1.29	35 $\pm$ 11 $\pm$ 5	41 $\pm$ 10 $\pm$ 9	47 $\pm$ 10 $\pm$ 4	70.0 $\pm$ 9.4 $\pm$ 4.7	58 $\pm$ 19 $\pm$ 7	
1.31	29 $\pm$ 10 $\pm$ 5	51 $\pm$ 10 $\pm$ 5	49.2 $\pm$ 9.0 $\pm$ 3.1	58.3 $\pm$ 8.8 $\pm$ 3.7		
1.33	29.3 $\pm$ 8.5 $\pm$ 2.5	44 $\pm$ 10 $\pm$ 4	35.0 $\pm$ 6.6 $\pm$ 4.3	39.8 $\pm$ 8.8 $\pm$ 2.7		
1.35	10.4 $\pm$ 5.0 $\pm$ 7.7	28.9 $\pm$ 9.7 $\pm$ 4.6	31.2 $\pm$ 5.4 $\pm$ 3.3	43 $\pm$ 11 $\pm$ 10	52 $\pm$ 19 $\pm$ 22	
1.37	24.0 $\pm$ 9.9 $\pm$ 5.9	57 $\pm$ 12 $\pm$ 4	45.0 $\pm$ 6.3 $\pm$ 4.1	38 $\pm$ 12 $\pm$ 4	24 $\pm$ 18 $\pm$ 7	
1.39		42.1 $\pm$ 7.5 $\pm$ 7.4	35.9 $\pm$ 6.2 $\pm$ 2.3	31 $\pm$ 10 $\pm$ 6		
1.41	12 $\pm$ 10 $\pm$ 13	21.3 $\pm$ 4.8 $\pm$ 7.8	30.8 $\pm$ 6.9 $\pm$ 1.8	18.0 $\pm$ 9.1 $\pm$ 4.1	69 $\pm$ 37 $\pm$ 8	
1.43	28.6 $\pm$ 8.0 $\pm$ 6.1	32.1 $\pm$ 5.7 $\pm$ 4.2	27.6 $\pm$ 8.0 $\pm$ 6.6	25 $\pm$ 11 $\pm$ 6	48 $\pm$ 21 $\pm$ 12	
1.45	27.8 $\pm$ 6.5 $\pm$ 4.0	36.9 $\pm$ 7.3 $\pm$ 8.8	31.3 $\pm$ 8.6 $\pm$ 5.5	11 $\pm$ 8 $\pm$ 10		
1.47		44 $\pm$ 11 $\pm$ 8	25 $\pm$ 7 $\pm$ 10	49 $\pm$ 12 $\pm$ 9		
1.49		47 $\pm$ 14 $\pm$ 14	46 $\pm$ 10 $\pm$ 6	70 $\pm$ 14 $\pm$ 8		
1.51		38 $\pm$ 10 $\pm$ 6	57 $\pm$ 10 $\pm$ 5	50 $\pm$ 12 $\pm$ 16		
1.53		40 $\pm$ 11 $\pm$ 6	53 $\pm$ 10 $\pm$ 3	37 $\pm$ 10 $\pm$ 12		
1.55		30 $\pm$ 13 $\pm$ 16	45.2 $\pm$ 8.4 $\pm$ 2.6	42 $\pm$ 10 $\pm$ 6		
1.57			36.7 $\pm$ 7.8 $\pm$ 6.8	59 $\pm$ 12 $\pm$ 5		
1.59		15.5 $\pm$ 7.3 $\pm$ 9.9	22.1 $\pm$ 6.7 $\pm$ 3.6	37 $\pm$ 12 $\pm$ 4		
1.61		12.8 $\pm$ 6.7 $\pm$ 6.5	28.4 $\pm$ 7.4 $\pm$ 3.3	30 $\pm$ 11 $\pm$ 3		
1.63			47.3 $\pm$ 9.1 $\pm$ 4.3	32 $\pm$ 12 $\pm$ 6		
1.65			48.9 $\pm$ 9.7 $\pm$ 6.0	27 $\pm$ 14 $\pm$ 5		
1.67			18.1 $\pm$ 7.4 $\pm$ 7.1	47 $\pm$ 13 $\pm$ 15		
1.69			12.6 $\pm$ 9.1 $\pm$ 9.4			

TABLE III:  $H(e, e'p)\gamma$  cross section  $d^5\sigma/(dk'_{lab} d[\Omega_e]_{lab} d[\Omega_p]_{c.m.})$  ( $\pm$  statistical  $\pm$  systematic error) at  $Q^2=1.0$  GeV<sup>2</sup> and  $\cos\theta_{\gamma\gamma}^* = -0.650$ , in fb/(MeV  $\cdot$  sr<sup>2</sup>).

$W$ (GeV)	$\phi = 15^\circ$	$\phi = 45^\circ$	$\phi = 75^\circ$	$\phi = 105^\circ$	$\phi = 135^\circ$	$\phi = 165^\circ$
0.99			554 $\pm$ 216 $\pm$ 88	452 $\pm$ 90 $\pm$ 38	454 $\pm$ 64 $\pm$ 23	340 $\pm$ 49 $\pm$ 26
1.01	4710 $\pm$ 1720 $\pm$ 565	1400 $\pm$ 552 $\pm$ 135	380 $\pm$ 87 $\pm$ 71	286 $\pm$ 46 $\pm$ 17	213 $\pm$ 30 $\pm$ 16	274 $\pm$ 31 $\pm$ 17
1.03	2760 $\pm$ 1140 $\pm$ 430	237 $\pm$ 109 $\pm$ 55	270 $\pm$ 50 $\pm$ 18	195 $\pm$ 28 $\pm$ 16	234 $\pm$ 27 $\pm$ 12	205 $\pm$ 25 $\pm$ 11
1.05		277 $\pm$ 94 $\pm$ 63	234 $\pm$ 41 $\pm$ 12	211 $\pm$ 27 $\pm$ 16	167 $\pm$ 22 $\pm$ 14	173 $\pm$ 22 $\pm$ 9
1.07		65 $\pm$ 36 $\pm$ 19	183 $\pm$ 29 $\pm$ 8	161 $\pm$ 21 $\pm$ 10	140 $\pm$ 18 $\pm$ 11	142 $\pm$ 19 $\pm$ 20
1.09		266 $\pm$ 59 $\pm$ 12	153 $\pm$ 24 $\pm$ 9	169 $\pm$ 20 $\pm$ 9	139 $\pm$ 19 $\pm$ 10	97 $\pm$ 21 $\pm$ 101
1.11		189 $\pm$ 44 $\pm$ 18	139 $\pm$ 21 $\pm$ 5	108 $\pm$ 15 $\pm$ 7	152 $\pm$ 26 $\pm$ 41	
1.13	462 $\pm$ 181 $\pm$ 270	195 $\pm$ 41 $\pm$ 9	113 $\pm$ 17 $\pm$ 5	123 $\pm$ 18 $\pm$ 7		
1.15	131 $\pm$ 69 $\pm$ 97	92 $\pm$ 26 $\pm$ 9	102 $\pm$ 15 $\pm$ 5	125 $\pm$ 20 $\pm$ 11	128 $\pm$ 27 $\pm$ 169	
1.17	134 $\pm$ 57 $\pm$ 65	132 $\pm$ 27 $\pm$ 13	95 $\pm$ 15 $\pm$ 10	135 $\pm$ 21 $\pm$ 15		
1.19	196 $\pm$ 52 $\pm$ 3	107 $\pm$ 22 $\pm$ 24	168 $\pm$ 20 $\pm$ 5	152 $\pm$ 22 $\pm$ 27		
1.21		154 $\pm$ 25 $\pm$ 22	153 $\pm$ 18 $\pm$ 14	125 $\pm$ 21 $\pm$ 17		
1.23		104 $\pm$ 19 $\pm$ 16	132 $\pm$ 17 $\pm$ 10	87 $\pm$ 21 $\pm$ 10		
1.25		108 $\pm$ 19 $\pm$ 12	76 $\pm$ 13 $\pm$ 12	50 $\pm$ 15 $\pm$ 59		
1.27		107 $\pm$ 20 $\pm$ 11	103 $\pm$ 15 $\pm$ 15	85 $\pm$ 16 $\pm$ 73		
1.29		51 $\pm$ 17 $\pm$ 6	79 $\pm$ 15 $\pm$ 15	43 $\pm$ 10 $\pm$ 12		
1.31		77 $\pm$ 19 $\pm$ 23	69 $\pm$ 13 $\pm$ 14	68 $\pm$ 14 $\pm$ 32		
1.33		60 $\pm$ 16 $\pm$ 16	42 $\pm$ 10 $\pm$ 15	54 $\pm$ 15 $\pm$ 42		
1.35		62 $\pm$ 16 $\pm$ 4	65 $\pm$ 11 $\pm$ 3			
1.37		59 $\pm$ 18 $\pm$ 11	29 $\pm$ 7 $\pm$ 16			
1.39			43 $\pm$ 8 $\pm$ 25			
1.41			45 $\pm$ 10 $\pm$ 23			
1.43			36 $\pm$ 11 $\pm$ 18			

TABLE IV:  $H(e, e'p)\gamma$  cross section  $d^5\sigma/(dk'_{lab} d[\Omega_e]_{lab} d[\Omega_p]_{c.m.})$  ( $\pm$  statistical error) at  $\cos\theta_{\gamma\gamma}^* = -0.975$  and  $W = 1.45, 1.47, 1.49, 1.51$  GeV, in  $\text{fb}/(\text{MeV} \cdot \text{sr}^2)$ . The systematic error is globally  $\pm 12\%$  on each point.

$W$ (GeV)	$Q^2$ (GeV <sup>2</sup> )	$\phi = 15^\circ$	$\phi = 45^\circ$	$\phi = 75^\circ$	$\phi = 105^\circ$	$\phi = 135^\circ$	$\phi = 165^\circ$
1.45	0.700						153 $\pm$ 61
1.45	0.875	58 $\pm$ 47	49 $\pm$ 24	43 $\pm$ 17	124 $\pm$ 46		
1.45	0.925		17 $\pm$ 12	26 $\pm$ 12	98 $\pm$ 43		
1.45	0.975	34 $\pm$ 17	16.2 $\pm$ 9.8	30 $\pm$ 11	137 $\pm$ 102		
1.45	1.025		33 $\pm$ 16	49 $\pm$ 17	12.6 $\pm$ 9.3	35 $\pm$ 12	62 $\pm$ 19
1.45	1.075				28.4 $\pm$ 9.7	31.1 $\pm$ 9.3	18 $\pm$ 10
1.45	1.125				19.8 $\pm$ 8.4	15.1 $\pm$ 7.7	24 $\pm$ 13
1.45	2.150			9.5 $\pm$ 5.6	2.3 $\pm$ 1.2	2.9 $\pm$ 1.2	2.0 $\pm$ 1.4
1.47	0.633				1040 $\pm$ 909	119 $\pm$ 117	
1.47	0.700				84 $\pm$ 79	145 $\pm$ 38	72 $\pm$ 36
1.47	0.767						156 $\pm$ 95
1.47	0.875	31 $\pm$ 24	60 $\pm$ 18	49 $\pm$ 17			
1.47	0.925	73 $\pm$ 21	46 $\pm$ 14	48 $\pm$ 18			
1.47	0.975	40 $\pm$ 19	19 $\pm$ 10	44 $\pm$ 22	61 $\pm$ 17	48 $\pm$ 17	29 $\pm$ 19
1.47	1.025			40 $\pm$ 17	28.6 $\pm$ 9.4	37 $\pm$ 11	46 $\pm$ 19
1.47	1.075	154 $\pm$ 111		63 $\pm$ 21	27.5 $\pm$ 8.7	22 $\pm$ 10	34 $\pm$ 18
1.47	1.125			22 $\pm$ 13	14.1 $\pm$ 7.0	46 $\pm$ 16	25 $\pm$ 19
1.47	2.050				3.5 $\pm$ 1.6	1.7 $\pm$ 1.1	4.1 $\pm$ 2.4
1.47	2.150			2.0 $\pm$ 1.5	2.2 $\pm$ 1.1	2.2 $\pm$ 1.6	2.4 $\pm$ 1.5
1.49	0.567					3280 $\pm$ 2850	2500 $\pm$ 2110
1.49	0.633				335 $\pm$ 75	124 $\pm$ 46	169 $\pm$ 61
1.49	0.700				140 $\pm$ 46	82 $\pm$ 31	98 $\pm$ 45
1.49	0.767				124 $\pm$ 92	144 $\pm$ 75	108 $\pm$ 112
1.49	0.875	39 $\pm$ 15	83 $\pm$ 18	51 $\pm$ 26			
1.49	0.925	89 $\pm$ 23	56 $\pm$ 17	76 $\pm$ 23	44 $\pm$ 17	63 $\pm$ 28	86 $\pm$ 43
1.49	0.975	66 $\pm$ 37	77 $\pm$ 36	44 $\pm$ 14	40 $\pm$ 11	25 $\pm$ 14	29 $\pm$ 23
1.49	1.025	95 $\pm$ 51	26 $\pm$ 21	68 $\pm$ 15	41 $\pm$ 10	63 $\pm$ 21	30 $\pm$ 24
1.49	1.075		42 $\pm$ 24	46 $\pm$ 12	40 $\pm$ 10	21 $\pm$ 19	57 $\pm$ 27
1.49	1.125			24 $\pm$ 11	8.0 $\pm$ 8.1	42 $\pm$ 11	51 $\pm$ 10
1.49	1.950			24 $\pm$ 14	6.2 $\pm$ 4.4		5.8 $\pm$ 3.5
1.49	2.050		8.2 $\pm$ 5.9	2.2 $\pm$ 1.4	2.2 $\pm$ 1.1	5.1 $\pm$ 1.6	3.1 $\pm$ 1.5
1.49	2.150		9.1 $\pm$ 6.5	2.8 $\pm$ 1.4	2.5 $\pm$ 1.8		
1.51	0.567		488 $\pm$ 318	370 $\pm$ 137	151 $\pm$ 77	332 $\pm$ 126	465 $\pm$ 267
1.51	0.633		483 $\pm$ 379	129 $\pm$ 82	207 $\pm$ 39	204 $\pm$ 53	171 $\pm$ 74
1.51	0.700			159 $\pm$ 145	88 $\pm$ 29	150 $\pm$ 46	112 $\pm$ 65
1.51	0.767				98 $\pm$ 80	227 $\pm$ 157	808 $\pm$ 674
1.51	0.875	55 $\pm$ 15	26 $\pm$ 11	42 $\pm$ 24	99 $\pm$ 31		
1.51	0.925	33 $\pm$ 19	56 $\pm$ 19	35 $\pm$ 12	49 $\pm$ 14	55 $\pm$ 33	277 $\pm$ 104
1.51	0.975	54 $\pm$ 25	59 $\pm$ 20	76 $\pm$ 14	64 $\pm$ 16	50 $\pm$ 35	106 $\pm$ 73
1.51	1.025		25 $\pm$ 13	36.9 $\pm$ 9.8	34 $\pm$ 13		
1.51	1.075	128 $\pm$ 66	54 $\pm$ 22	30 $\pm$ 10	55 $\pm$ 13	27.3 $\pm$ 8.5	68 $\pm$ 13
1.51	1.125			62 $\pm$ 36	13.4 $\pm$ 7.6	42.6 $\pm$ 8.6	52 $\pm$ 10
1.51	1.950				4.2 $\pm$ 1.8	8.4 $\pm$ 2.6	2.5 $\pm$ 1.6
1.51	2.050			5.3 $\pm$ 1.7	4.1 $\pm$ 1.4	2.0 $\pm$ 1.2	3.3 $\pm$ 2.2
1.51	2.150	9.1 $\pm$ 6.6			5.2 $\pm$ 3.1		

TABLE V:  $H(e, e'p)\gamma$  cross section  $d^5\sigma/(dk'_{lab} d[\Omega_e]_{lab} d[\Omega_p]_{c.m.})$  ( $\pm$  statistical error) at  $\cos\theta_{\gamma\gamma}^* = -0.975$  and  $W = 1.53, 1.55, 1.57, 1.59$  GeV, in  $\text{fb}/(\text{MeV} \cdot \text{sr}^2)$ . The systematic error is globally  $\pm 12\%$  on each point.

$W$ (GeV)	$Q^2$ (GeV <sup>2</sup> )	$\phi = 15^\circ$	$\phi = 45^\circ$	$\phi = 75^\circ$	$\phi = 105^\circ$	$\phi = 135^\circ$	$\phi = 165^\circ$
1.53	0.500	405 $\pm$ 383	449 $\pm$ 312	346 $\pm$ 199	907 $\pm$ 472		
1.53	0.567	50 $\pm$ 95	145 $\pm$ 91	68 $\pm$ 43	146 $\pm$ 45	382 $\pm$ 134	258 $\pm$ 173
1.53	0.633		192 $\pm$ 135	165 $\pm$ 45	117 $\pm$ 33	103 $\pm$ 66	461 $\pm$ 165
1.53	0.700		361 $\pm$ 304	62 $\pm$ 56	87 $\pm$ 33	170 $\pm$ 94	260 $\pm$ 164
1.53	0.875	70 $\pm$ 17	63 $\pm$ 17	55 $\pm$ 16	64 $\pm$ 25		
1.53	0.925	56 $\pm$ 20	10.1 $\pm$ 9.1	38 $\pm$ 11	31 $\pm$ 18		
1.53	0.975	33 $\pm$ 14	81 $\pm$ 17	30.9 $\pm$ 9.3	67 $\pm$ 27		95 $\pm$ 70
1.53	1.025	26 $\pm$ 14	31 $\pm$ 12	49 $\pm$ 12	42 $\pm$ 12	52 $\pm$ 12	46 $\pm$ 14
1.53	1.075		81 $\pm$ 58	47 $\pm$ 24	40.0 $\pm$ 9.2	17.0 $\pm$ 6.2	22.4 $\pm$ 8.8
1.53	1.125				15.0 $\pm$ 6.2	17.4 $\pm$ 6.3	36 $\pm$ 11
1.53	1.850				11.2 $\pm$ 7.2		
1.53	1.950		4.3 $\pm$ 2.7	2.9 $\pm$ 1.4	4.5 $\pm$ 1.6	3.0 $\pm$ 1.6	2.6 $\pm$ 1.9
1.53	2.050			3.3 $\pm$ 1.3	1.5 $\pm$ 0.9		
1.53	2.150	7.2 $\pm$ 5.1	3.8 $\pm$ 2.3		4.6 $\pm$ 3.3		
1.55	0.500	315 $\pm$ 181	290 $\pm$ 144	235 $\pm$ 69	236 $\pm$ 126		
1.55	0.567	221 $\pm$ 75	268 $\pm$ 69	170 $\pm$ 39	261 $\pm$ 63	621 $\pm$ 511	2290 $\pm$ 1550
1.55	0.633	137 $\pm$ 129	171 $\pm$ 69	75 $\pm$ 30	100 $\pm$ 43	588 $\pm$ 401	
1.55	0.700			123 $\pm$ 116	77 $\pm$ 104		
1.55	0.875	48 $\pm$ 16	50 $\pm$ 13	28 $\pm$ 10	99 $\pm$ 75		
1.55	0.925	54 $\pm$ 15	36 $\pm$ 10	45 $\pm$ 12			
1.55	0.975	39 $\pm$ 14	30 $\pm$ 10	20.8 $\pm$ 8.8	37 $\pm$ 11	57 $\pm$ 14	54 $\pm$ 18
1.55	1.025	147 $\pm$ 71	48 $\pm$ 23	10.9 $\pm$ 7.2	41.3 $\pm$ 8.8	48 $\pm$ 10	80 $\pm$ 18
1.55	1.075		63 $\pm$ 44	46 $\pm$ 15	31.6 $\pm$ 7.6	61 $\pm$ 12	27 $\pm$ 13
1.55	1.125			19 $\pm$ 10	20.1 $\pm$ 6.3	22.5 $\pm$ 9.1	29 $\pm$ 16
1.55	1.850			9.3 $\pm$ 6.6	6.6 $\pm$ 3.1		
1.55	1.950		2.3 $\pm$ 1.4	1.2 $\pm$ 0.7	2.0 $\pm$ 1.0	6.0 $\pm$ 4.3	
1.55	2.050		2.0 $\pm$ 1.1	4.5 $\pm$ 1.5	2.6 $\pm$ 1.6		
1.57	0.500	257 $\pm$ 78	146 $\pm$ 57	400 $\pm$ 69			
1.57	0.567	97 $\pm$ 79	155 $\pm$ 47	191 $\pm$ 38			
1.57	0.633	146 $\pm$ 142	101 $\pm$ 85	37 $\pm$ 35	476 $\pm$ 247		
1.57	0.875	30 $\pm$ 10	30.6 $\pm$ 9.4	49 $\pm$ 15			
1.57	0.925	25.3 $\pm$ 9.9	40 $\pm$ 10	36 $\pm$ 12	50 $\pm$ 14	52 $\pm$ 18	37 $\pm$ 26
1.57	0.975	46 $\pm$ 28	36 $\pm$ 19	36 $\pm$ 10	39.1 $\pm$ 8.8	44 $\pm$ 13	45 $\pm$ 21
1.57	1.025	65 $\pm$ 46		26.4 $\pm$ 8.5	25.5 $\pm$ 7.1	17 $\pm$ 10	27 $\pm$ 18
1.57	1.075		34 $\pm$ 17	21.8 $\pm$ 7.5	39.9 $\pm$ 8.8	29 $\pm$ 13	22 $\pm$ 21
1.57	1.125			20.5 $\pm$ 7.9	18.8 $\pm$ 7.2	37 $\pm$ 16	21 $\pm$ 14
1.57	1.850		3.1 $\pm$ 2.3	1.8 $\pm$ 1.2	5.4 $\pm$ 3.3	13.5 $\pm$ 9.7	
1.57	1.950	2.4 $\pm$ 1.3	3.0 $\pm$ 1.2	4.7 $\pm$ 1.5	3.4 $\pm$ 1.8		
1.57	2.050			2.3 $\pm$ 1.4			
1.59	0.433		121 $\pm$ 177	440 $\pm$ 410			
1.59	0.500	118 $\pm$ 58	141 $\pm$ 48	187 $\pm$ 73			
1.59	0.567	117 $\pm$ 63	64 $\pm$ 38	173 $\pm$ 56			
1.59	0.633		6070 $\pm$ 6330				
1.59	0.875	26.6 $\pm$ 8.2	37.4 $\pm$ 9.0	45 $\pm$ 16	49 $\pm$ 18	93 $\pm$ 45	156 $\pm$ 129
1.59	0.925	74 $\pm$ 23	46 $\pm$ 13	26.1 $\pm$ 9.3	53 $\pm$ 12	14 $\pm$ 14	108 $\pm$ 78
1.59	0.975	33 $\pm$ 22	30 $\pm$ 12	27.9 $\pm$ 7.8	35.1 $\pm$ 9.3	32 $\pm$ 30	54 $\pm$ 42
1.59	1.025	21 $\pm$ 18	32 $\pm$ 11	29.1 $\pm$ 7.5	44 $\pm$ 10		
1.59	1.075	23 $\pm$ 14	34 $\pm$ 14	30.0 $\pm$ 7.7	38 $\pm$ 11	60 $\pm$ 24	29 $\pm$ 14
1.59	1.125			56 $\pm$ 22	16 $\pm$ 11	18.8 $\pm$ 6.3	12.2 $\pm$ 5.5
1.59	1.850		2.0 $\pm$ 1.3	1.7 $\pm$ 1.0	5.8 $\pm$ 2.6		
1.59	1.950		2.5 $\pm$ 1.5	2.0 $\pm$ 1.5			



TABLE VI:  $H(e, e'p)\pi^0$  two-fold cross section  $d^2\sigma/d[\Omega_p]_{\text{c.m.}}$  ( $\pm$  statistical error) at  $\cos\theta_{\text{c.m.}} = -0.975$  and  $W = 1.45, 1.47, 1.49, 1.51$  GeV, in nb/sr. The systematic error is globally  $\pm 4\%$  on each point.

$W$ (GeV)	$Q^2$ (GeV <sup>2</sup> )	$\phi = 15^\circ$		$\phi = 45^\circ$		$\phi = 75^\circ$		$\phi = 105^\circ$		$\phi = 135^\circ$		$\phi = 165^\circ$							
1.45	0.700									788	$\pm$	498	289	$\pm$	158				
1.45	0.767									407	$\pm$	120	590	$\pm$	148				
1.45	0.875	120	$\pm$	28	105	$\pm$	23	268	$\pm$	34	167	$\pm$	51						
1.45	0.925	105	$\pm$	16	134	$\pm$	16	201	$\pm$	18	355	$\pm$	51	771	$\pm$	497	561	$\pm$	445
1.45	0.975	128	$\pm$	17	154	$\pm$	15	239	$\pm$	19	230	$\pm$	56	1360	$\pm$	1090			
1.45	1.025	184	$\pm$	22	144	$\pm$	16	252	$\pm$	22	167	$\pm$	48	327	$\pm$	77	532	$\pm$	113
1.45	1.075	177	$\pm$	33	195	$\pm$	26	210	$\pm$	25	266	$\pm$	24	395	$\pm$	30	423	$\pm$	38
1.45	1.125	150	$\pm$	102	157	$\pm$	82	246	$\pm$	48	315	$\pm$	24	382	$\pm$	28	461	$\pm$	42
1.45	2.050																267	$\pm$	186
1.45	2.150				314	$\pm$	146	103	$\pm$	26	91	$\pm$	16	130	$\pm$	18	164	$\pm$	21
1.45	2.250										124	$\pm$	49	71	$\pm$	35	96	$\pm$	44
1.47	0.700									497	$\pm$	87	525	$\pm$	43	663	$\pm$	51	
1.47	0.767									272	$\pm$	95	475	$\pm$	63	653	$\pm$	91	
1.47	0.875	209	$\pm$	23	166	$\pm$	17	209	$\pm$	21	483	$\pm$	308						
1.47	0.925	120	$\pm$	15	167	$\pm$	15	236	$\pm$	23	918	$\pm$	770						
1.47	0.975	174	$\pm$	19	220	$\pm$	19	257	$\pm$	28	194	$\pm$	84	402	$\pm$	104	299	$\pm$	104
1.47	1.025	154	$\pm$	22	235	$\pm$	23	225	$\pm$	23	334	$\pm$	26	411	$\pm$	34	523	$\pm$	53
1.47	1.075	138	$\pm$	51	179	$\pm$	41	229	$\pm$	25	295	$\pm$	20	439	$\pm$	31	642	$\pm$	59
1.47	1.125	84	$\pm$	66	191	$\pm$	50	223	$\pm$	26	320	$\pm$	23	502	$\pm$	44	523	$\pm$	66
1.47	2.050							33	$\pm$	19	94	$\pm$	24	206	$\pm$	35	178	$\pm$	32
1.47	2.150	35	$\pm$	21	78	$\pm$	24	65	$\pm$	12	134	$\pm$	15	165	$\pm$	18	189	$\pm$	23
1.47	2.250							108	$\pm$	68	447	$\pm$	209	102	$\pm$	73			
1.49	0.633									530	$\pm$	69	667	$\pm$	66	802	$\pm$	88	
1.49	0.700									528	$\pm$	35	605	$\pm$	30	695	$\pm$	43	
1.49	0.767									451	$\pm$	74	488	$\pm$	65	440	$\pm$	95	
1.49	0.875	164	$\pm$	15	198	$\pm$	16	283	$\pm$	33									
1.49	0.925	145	$\pm$	15	209	$\pm$	18	260	$\pm$	39	344	$\pm$	109	969	$\pm$	270	436	$\pm$	201
1.49	0.975	145	$\pm$	17	230	$\pm$	20	231	$\pm$	22	363	$\pm$	27	510	$\pm$	51	544	$\pm$	77
1.49	1.025	146	$\pm$	31	155	$\pm$	24	272	$\pm$	20	327	$\pm$	21	485	$\pm$	44	437	$\pm$	64
1.49	1.075	132	$\pm$	33	151	$\pm$	27	245	$\pm$	19	354	$\pm$	23	351	$\pm$	44	460	$\pm$	80
1.49	1.125	128	$\pm$	33	133	$\pm$	26	248	$\pm$	22	375	$\pm$	29	427	$\pm$	55	304	$\pm$	50
1.49	1.950													543	$\pm$	324			
1.49	2.050				52	$\pm$	19	70	$\pm$	13	98	$\pm$	13	145	$\pm$	17	218	$\pm$	25
1.49	2.150	34	$\pm$	15	68	$\pm$	16	88	$\pm$	12	97	$\pm$	13	154	$\pm$	22	135	$\pm$	28
1.51	0.567	706	$\pm$	555	426	$\pm$	351	679	$\pm$	187	664	$\pm$	136	878	$\pm$	179	1020	$\pm$	276
1.51	0.633	410	$\pm$	173	495	$\pm$	146	490	$\pm$	52	617	$\pm$	29	717	$\pm$	39	721	$\pm$	56
1.51	0.700	463	$\pm$	353	552	$\pm$	325	481	$\pm$	84	584	$\pm$	27	702	$\pm$	38	680	$\pm$	57
1.51	0.767							1200	$\pm$	496	496	$\pm$	61	470	$\pm$	84	821	$\pm$	196
1.51	0.875	248	$\pm$	17	283	$\pm$	19	371	$\pm$	67	249	$\pm$	111	1270	$\pm$	552	876	$\pm$	514
1.51	0.925	248	$\pm$	19	285	$\pm$	22	347	$\pm$	28	441	$\pm$	35	522	$\pm$	81	495	$\pm$	124
1.51	0.975	234	$\pm$	29	301	$\pm$	27	345	$\pm$	20	441	$\pm$	27	527	$\pm$	73	478	$\pm$	102
1.51	1.025	240	$\pm$	33	252	$\pm$	25	330	$\pm$	19	428	$\pm$	28	468	$\pm$	81	574	$\pm$	139
1.51	1.075	170	$\pm$	27	266	$\pm$	27	350	$\pm$	22	320	$\pm$	28	372	$\pm$	55	431	$\pm$	66
1.51	1.125	244	$\pm$	53	185	$\pm$	32	316	$\pm$	28	391	$\pm$	29	424	$\pm$	25	529	$\pm$	31
1.51	1.950	76	$\pm$	38	115	$\pm$	41	132	$\pm$	30	84	$\pm$	20	144	$\pm$	28	199	$\pm$	39
1.51	2.050	51	$\pm$	15	96	$\pm$	17	120	$\pm$	13	146	$\pm$	13	173	$\pm$	18	169	$\pm$	24
1.51	2.150	30	$\pm$	12	79	$\pm$	15	84	$\pm$	13	116	$\pm$	17	115	$\pm$	30	197	$\pm$	58

TABLE VII:  $H(e, e'p)\pi^0$  two-fold cross section  $d^2\sigma/d[\Omega_p]_{\text{c.m.}}$  ( $\pm$  statistical error) at  $\cos\theta_{\text{c.m.}} = -0.975$  and  $W = 1.53, 1.55, 1.57, 1.59$  GeV, in nb/sr. The systematic error is globally  $\pm 4\%$  on each point.

$W$ (GeV)	$Q^2$ (GeV <sup>2</sup> )	$\phi = 15^\circ$		$\phi = 45^\circ$		$\phi = 75^\circ$		$\phi = 105^\circ$		$\phi = 135^\circ$		$\phi = 165^\circ$	
1.53	0.567	248	$\pm$ 53	409	$\pm$ 54	503	$\pm$ 34	580	$\pm$ 34	600	$\pm$ 70	406	$\pm$ 81
1.53	0.633	385	$\pm$ 79	499	$\pm$ 69	510	$\pm$ 30	578	$\pm$ 24	522	$\pm$ 45	557	$\pm$ 70
1.53	0.700	296	$\pm$ 120	336	$\pm$ 91	448	$\pm$ 38	561	$\pm$ 28	519	$\pm$ 55	519	$\pm$ 85
1.53	0.767					384	$\pm$ 146	427	$\pm$ 76	441	$\pm$ 195	890	$\pm$ 506
1.53	0.875	311	$\pm$ 19	299	$\pm$ 22	409	$\pm$ 34	403	$\pm$ 52	291	$\pm$ 149	2850	$\pm$ 1830
1.53	0.925	269	$\pm$ 26	313	$\pm$ 23	360	$\pm$ 20	510	$\pm$ 42	501	$\pm$ 159	630	$\pm$ 278
1.53	0.975	262	$\pm$ 27	340	$\pm$ 23	430	$\pm$ 22	368	$\pm$ 37	148	$\pm$ 103	1320	$\pm$ 806
1.53	1.025	285	$\pm$ 29	344	$\pm$ 24	365	$\pm$ 21	419	$\pm$ 44	229	$\pm$ 46	282	$\pm$ 56
1.53	1.075	357	$\pm$ 46	294	$\pm$ 28	358	$\pm$ 25	366	$\pm$ 23	407	$\pm$ 24	407	$\pm$ 29
1.53	1.125	175	$\pm$ 130	294	$\pm$ 91	339	$\pm$ 48	400	$\pm$ 22	392	$\pm$ 22	396	$\pm$ 29
1.53	1.850	1030	$\pm$ 804			514	$\pm$ 380						
1.53	1.950	83	$\pm$ 23	164	$\pm$ 27	156	$\pm$ 18	126	$\pm$ 14	179	$\pm$ 21	126	$\pm$ 23
1.53	2.050	103	$\pm$ 17	135	$\pm$ 16	174	$\pm$ 14	163	$\pm$ 15	143	$\pm$ 22	117	$\pm$ 28
1.53	2.150	116	$\pm$ 25	122	$\pm$ 21	94	$\pm$ 17	176	$\pm$ 33	263	$\pm$ 97	166	$\pm$ 106
1.55	0.500	286	$\pm$ 49	447	$\pm$ 53	511	$\pm$ 46	622	$\pm$ 97	879	$\pm$ 504	3240	$\pm$ 2290
1.55	0.567	328	$\pm$ 37	436	$\pm$ 32	503	$\pm$ 21	474	$\pm$ 30	273	$\pm$ 88	272	$\pm$ 124
1.55	0.633	278	$\pm$ 46	345	$\pm$ 38	480	$\pm$ 23	487	$\pm$ 28	306	$\pm$ 79	365	$\pm$ 117
1.55	0.700	62	$\pm$ 70	258	$\pm$ 83	427	$\pm$ 37	412	$\pm$ 39	193	$\pm$ 114	274	$\pm$ 169
1.55	0.767							440	$\pm$ 454				
1.55	0.875	235	$\pm$ 18	301	$\pm$ 20	313	$\pm$ 19	271	$\pm$ 79				
1.55	0.925	237	$\pm$ 20	312	$\pm$ 19	403	$\pm$ 23	133	$\pm$ 57				
1.55	0.975	272	$\pm$ 22	334	$\pm$ 20	387	$\pm$ 24	339	$\pm$ 58	286	$\pm$ 60	302	$\pm$ 72
1.55	1.025	306	$\pm$ 30	358	$\pm$ 24	328	$\pm$ 21	318	$\pm$ 20	361	$\pm$ 25	225	$\pm$ 24
1.55	1.075	277	$\pm$ 71	244	$\pm$ 42	336	$\pm$ 27	339	$\pm$ 18	313	$\pm$ 21	274	$\pm$ 27
1.55	1.125	278	$\pm$ 102	189	$\pm$ 61	366	$\pm$ 32	298	$\pm$ 18	270	$\pm$ 23	243	$\pm$ 31
1.55	1.850	158	$\pm$ 79	138	$\pm$ 44	182	$\pm$ 35	101	$\pm$ 24	107	$\pm$ 29	134	$\pm$ 41
1.55	1.950	101	$\pm$ 17	116	$\pm$ 15	137	$\pm$ 13	144	$\pm$ 13	125	$\pm$ 20	62	$\pm$ 20
1.55	2.050	77	$\pm$ 12	121	$\pm$ 13	121	$\pm$ 12	145	$\pm$ 18	26	$\pm$ 18		
1.55	2.150	92	$\pm$ 31	138	$\pm$ 33	118	$\pm$ 32	83	$\pm$ 54				
1.57	0.433	342	$\pm$ 195	100	$\pm$ 147	293	$\pm$ 332						
1.57	0.500	421	$\pm$ 33	464	$\pm$ 28	548	$\pm$ 27	488	$\pm$ 145				
1.57	0.567	286	$\pm$ 28	422	$\pm$ 24	440	$\pm$ 19	407	$\pm$ 63				
1.57	0.633	284	$\pm$ 43	339	$\pm$ 33	474	$\pm$ 24	340	$\pm$ 57				
1.57	0.700	324	$\pm$ 414	299	$\pm$ 205	431	$\pm$ 85	327	$\pm$ 150				
1.57	0.875	222	$\pm$ 16	258	$\pm$ 14	333	$\pm$ 22						
1.57	0.925	254	$\pm$ 18	299	$\pm$ 17	341	$\pm$ 27	332	$\pm$ 67	145	$\pm$ 47	174	$\pm$ 73
1.57	0.975	275	$\pm$ 22	328	$\pm$ 19	316	$\pm$ 20	322	$\pm$ 20	286	$\pm$ 27	178	$\pm$ 30
1.57	1.025	180	$\pm$ 36	306	$\pm$ 33	301	$\pm$ 19	298	$\pm$ 16	234	$\pm$ 23	167	$\pm$ 28
1.57	1.075	238	$\pm$ 51	299	$\pm$ 42	300	$\pm$ 20	295	$\pm$ 16	220	$\pm$ 24	278	$\pm$ 40
1.57	1.125	194	$\pm$ 52	188	$\pm$ 36	282	$\pm$ 20	284	$\pm$ 20	222	$\pm$ 34	138	$\pm$ 37
1.57	1.850	117	$\pm$ 27	123	$\pm$ 22	165	$\pm$ 20	131	$\pm$ 18	84	$\pm$ 23	46	$\pm$ 33
1.57	1.950	78	$\pm$ 12	131	$\pm$ 13	119	$\pm$ 11	121	$\pm$ 14	97	$\pm$ 30	78	$\pm$ 36
1.57	2.050	87	$\pm$ 14	132	$\pm$ 15	123	$\pm$ 16	73	$\pm$ 23			1080	$\pm$ 823
1.59	0.433	592	$\pm$ 101	514	$\pm$ 84	605	$\pm$ 160						
1.59	0.500	457	$\pm$ 28	471	$\pm$ 23	571	$\pm$ 31						
1.59	0.567	414	$\pm$ 30	446	$\pm$ 22	456	$\pm$ 25						
1.59	0.633	398	$\pm$ 113	406	$\pm$ 62	463	$\pm$ 48						
1.59	0.875	282	$\pm$ 15	281	$\pm$ 13	244	$\pm$ 26	315	$\pm$ 83	99	$\pm$ 72	132	$\pm$ 95
1.59	0.925	315	$\pm$ 21	337	$\pm$ 20	372	$\pm$ 23	326	$\pm$ 24	231	$\pm$ 38	229	$\pm$ 48
1.59	0.975	330	$\pm$ 38	358	$\pm$ 29	354	$\pm$ 18	367	$\pm$ 20	210	$\pm$ 34	209	$\pm$ 46
1.59	1.025	298	$\pm$ 42	327	$\pm$ 30	314	$\pm$ 17	302	$\pm$ 19	277	$\pm$ 47	131	$\pm$ 42
1.59	1.075	311	$\pm$ 43	366	$\pm$ 35	350	$\pm$ 19	295	$\pm$ 21	240	$\pm$ 55	151	$\pm$ 59
1.59	1.125	195	$\pm$ 50	300	$\pm$ 42	310	$\pm$ 23	245	$\pm$ 26	212	$\pm$ 26	145	$\pm$ 20
1.59	1.750			257	$\pm$ 124	115	$\pm$ 61	200	$\pm$ 96				
1.59	1.850	129	$\pm$ 19	124	$\pm$ 15	166	$\pm$ 15	133	$\pm$ 17	120	$\pm$ 44	285	$\pm$ 133
1.59	1.950	121	$\pm$ 13	143	$\pm$ 12	132	$\pm$ 12	139	$\pm$ 27				
1.59	2.050	49	$\pm$ 28	208	$\pm$ 52	174	$\pm$ 67						

TABLE VIII: The reduced cross section  $\langle d^2\sigma \rangle$  ( $\pm$  statistical error) as a function of  $Q^2$ , at  $W = 1.53$  GeV and  $\cos\theta_{e.m.} = -0.975$ , for the two processes  $H(e, e'p)\gamma$  and  $H(e, e'p)\pi^0$ . The systematic error on each cross-section point is globally  $\pm 15\%$  for the  $H(e, e'p)\gamma$  process and  $\pm 4\%$  for the  $H(e, e'p)\pi^0$  process.

$Q^2$ (GeV <sup>2</sup> )	$\langle d^2\sigma_\gamma \rangle$ (nb/sr)			$\langle d^2\sigma_{\pi^0} \rangle$ (nb/sr)		
0.567	35.4	$\pm$	7.0	480.9	$\pm$	18.6
0.633	30.5	$\pm$	5.4	499.9	$\pm$	15.0
0.700	25.9	$\pm$	13.2	468.8	$\pm$	18.2
0.767				383.6	$\pm$	57.1
0.875	23.7	$\pm$	4.1	394.9	$\pm$	15.7
0.925	20.4	$\pm$	3.8	382.4	$\pm$	14.0
0.975	27.3	$\pm$	4.0	393.6	$\pm$	14.3
1.025	22.2	$\pm$	3.4	352.4	$\pm$	13.5
1.075	20.7	$\pm$	3.0	347.1	$\pm$	10.6
1.125	16.0	$\pm$	3.0	338.1	$\pm$	11.7
1.950	7.8	$\pm$	2.1	131.9	$\pm$	7.9
2.050	8.6	$\pm$	2.4	149.4	$\pm$	7.5
2.150				136.0	$\pm$	12.6

TABLE IX: The ratio  $r$  of  $\gamma$  to  $\pi^0$  reduced cross sections ( $\pm$  statistical error), at  $Q^2 = 1 \text{ GeV}^2$  and  $\cos\theta_{\text{c.m.}} = -0.975$ . The next columns contain the reduced cross section  $\langle d^2\sigma_\gamma \rangle$  ( $\pm$  statistical  $\pm$  systematic error) at these kinematics, in terms of either  $\langle d^2\sigma_\gamma/d[\Omega_p]_{\text{c.m.}} \rangle$  or  $\langle d\sigma_\gamma/dt \rangle$ . The systematic error on  $\langle d\sigma \rangle$  is obtained by averaging over  $\phi$  the systematic error given in Table I.

$W$ (GeV)	$r = \langle d^2\sigma_\gamma \rangle / \langle d^2\sigma_{\pi^0} \rangle$			$\langle d^2\sigma_\gamma/d[\Omega_p]_{\text{c.m.}} \rangle$ (nb/sr)				$\langle d\sigma_\gamma/dt \rangle$ (nb/GeV <sup>2</sup> )					
0.99				497	$\pm$	67	$\pm$	283	28200	$\pm$	3810	$\pm$	16100
1.01				262	$\pm$	23	$\pm$	81	10900	$\pm$	995	$\pm$	3390
1.03				142	$\pm$	12	$\pm$	33	4750	$\pm$	411	$\pm$	1120
1.05				100	$\pm$	8	$\pm$	32	2800	$\pm$	242	$\pm$	906
1.07				88	$\pm$	7	$\pm$	19	2120	$\pm$	168	$\pm$	465
1.09				55	$\pm$	4	$\pm$	11	1180	$\pm$	103	$\pm$	247
1.11	0.3136	$\pm$	0.0315	60	$\pm$	4	$\pm$	10	1140	$\pm$	92	$\pm$	199
1.13	0.1083	$\pm$	0.0099	54.3	$\pm$	4.7	$\pm$	9.2	939	$\pm$	80	$\pm$	159
1.15	0.0644	$\pm$	0.0051	67	$\pm$	5	$\pm$	18	1070	$\pm$	82	$\pm$	288
1.17	0.0462	$\pm$	0.0030	91	$\pm$	5	$\pm$	10	1350	$\pm$	83	$\pm$	147
1.19	0.0309	$\pm$	0.0018	100	$\pm$	5	$\pm$	10	1370	$\pm$	76	$\pm$	143
1.21	0.0234	$\pm$	0.0013	94	$\pm$	5	$\pm$	10	1210	$\pm$	68	$\pm$	131
1.23	0.0212	$\pm$	0.0013	72.4	$\pm$	4.3	$\pm$	9.5	874	$\pm$	51	$\pm$	115
1.25	0.0212	$\pm$	0.0014	51.3	$\pm$	3.2	$\pm$	7.4	586	$\pm$	36	$\pm$	84
1.27	0.0192	$\pm$	0.0014	32.8	$\pm$	2.3	$\pm$	3.9	355	$\pm$	24	$\pm$	41
1.29	0.0188	$\pm$	0.0014	22.7	$\pm$	1.6	$\pm$	2.6	233	$\pm$	16	$\pm$	26
1.31	0.0239	$\pm$	0.0019	20.9	$\pm$	1.6	$\pm$	4.2	205	$\pm$	15	$\pm$	41
1.33	0.0264	$\pm$	0.0022	18.7	$\pm$	1.5	$\pm$	2.6	175	$\pm$	13	$\pm$	24
1.35	0.0292	$\pm$	0.0025	16.4	$\pm$	1.4	$\pm$	3.3	147	$\pm$	12	$\pm$	29
1.37	0.0277	$\pm$	0.0028	12.9	$\pm$	1.3	$\pm$	3.6	111	$\pm$	10	$\pm$	31
1.39	0.0354	$\pm$	0.0035	14.1	$\pm$	1.3	$\pm$	2.6	116	$\pm$	11	$\pm$	21
1.41	0.0444	$\pm$	0.0044	14.7	$\pm$	1.4	$\pm$	2.0	117	$\pm$	11	$\pm$	16
1.43	0.0441	$\pm$	0.0047	13.1	$\pm$	1.4	$\pm$	2.2	101	$\pm$	10	$\pm$	16
1.45	0.0594	$\pm$	0.0055	17.2	$\pm$	1.6	$\pm$	2.6	128	$\pm$	11	$\pm$	18
1.47	0.0677	$\pm$	0.0054	21.3	$\pm$	1.7	$\pm$	2.3	152	$\pm$	11	$\pm$	16
1.49	0.0874	$\pm$	0.0057	27.6	$\pm$	1.7	$\pm$	3.9	191	$\pm$	11	$\pm$	27
1.51	0.0722	$\pm$	0.0043	27.8	$\pm$	1.6	$\pm$	3.3	186	$\pm$	10	$\pm$	22
1.53	0.0616	$\pm$	0.0039	23.2	$\pm$	1.4	$\pm$	2.7	151	$\pm$	9	$\pm$	17
1.55	0.0704	$\pm$	0.0044	22.0	$\pm$	1.3	$\pm$	2.4	139	$\pm$	8	$\pm$	15
1.57	0.0659	$\pm$	0.0045	17.5	$\pm$	1.2	$\pm$	3.2	107	$\pm$	7	$\pm$	19
1.59	0.0700	$\pm$	0.0046	18.3	$\pm$	1.2	$\pm$	2.8	108	$\pm$	7	$\pm$	16
1.61	0.0503	$\pm$	0.0037	15.6	$\pm$	1.1	$\pm$	2.2	89	$\pm$	6	$\pm$	12
1.63	0.0427	$\pm$	0.0028	17.5	$\pm$	1.1	$\pm$	1.8	98	$\pm$	6	$\pm$	10
1.65	0.0306	$\pm$	0.0020	17.4	$\pm$	1.1	$\pm$	2.4	94	$\pm$	6	$\pm$	12
1.67	0.0180	$\pm$	0.0015	12.7	$\pm$	1.0	$\pm$	2.0	67	$\pm$	5	$\pm$	10
1.69	0.0165	$\pm$	0.0016	11.8	$\pm$	1.1	$\pm$	4.2	60	$\pm$	5	$\pm$	21
1.71	0.0141	$\pm$	0.0017	8.8	$\pm$	1.0	$\pm$	1.9	44.2	$\pm$	5.2	$\pm$	9.3
1.73	0.0149	$\pm$	0.0019	6.7	$\pm$	0.8	$\pm$	2.6	32	$\pm$	4	$\pm$	12
1.75	0.0167	$\pm$	0.0021	6.2	$\pm$	0.8	$\pm$	1.2	29.5	$\pm$	3.6	$\pm$	5.6
1.77	0.0153	$\pm$	0.0020	5.2	$\pm$	0.7	$\pm$	2.0	24.4	$\pm$	3.2	$\pm$	9.1
1.79	0.0160	$\pm$	0.0021	5.3	$\pm$	0.7	$\pm$	2.5	24	$\pm$	3	$\pm$	11
1.81	0.0199	$\pm$	0.0021	7.0	$\pm$	0.7	$\pm$	2.3	31	$\pm$	3	$\pm$	10
1.83	0.0156	$\pm$	0.0020	5.6	$\pm$	0.7	$\pm$	2.0	24.0	$\pm$	3.1	$\pm$	8.7
1.85	0.0159	$\pm$	0.0020	5.7	$\pm$	0.7	$\pm$	1.1	23.9	$\pm$	3.0	$\pm$	4.9
1.87	0.0139	$\pm$	0.0021	4.8	$\pm$	0.7	$\pm$	1.2	19.7	$\pm$	2.9	$\pm$	4.9
1.89	0.0210	$\pm$	0.0025	6.7	$\pm$	0.8	$\pm$	2.6	27	$\pm$	3	$\pm$	10
1.91	0.0188	$\pm$	0.0028	5.5	$\pm$	0.8	$\pm$	1.7	21.7	$\pm$	3.2	$\pm$	6.5
1.93	0.0080	$\pm$	0.0029	2.1	$\pm$	0.8	$\pm$	0.6	8.1	$\pm$	3.0	$\pm$	2.4
1.95	0.0153	$\pm$	0.0043	3.4	$\pm$	1.0	$\pm$	1.0	12.9	$\pm$	3.6	$\pm$	3.9
1.97	0.0278	$\pm$	0.0093	5.2	$\pm$	1.7	$\pm$	1.6	19.1	$\pm$	6.4	$\pm$	5.7